Experimental Thermal and Fluid Science 148 (2023) 110963

Contents lists available at ScienceDirect

Experimental Thermal and Fluid Science

journal homepage: www.elsevier.com/locate/etfs

Inter-laboratory optical measurements of film thickness during annular flow condensation in a small diameter channel

Arianna Berto [a], Marion Beaumale [b], Pascal Lavieille [b], Marco Azzolin [a], Stefano Bortolin [a], Marc Miscevic [b], Davide Del Col [a,*]

[a] University of Padova, Department of Industrial Engineering, Via Venezia 1, 35131 Padova, Italy
[b] LAPLACE, Université de Toulouse, CNRS, INPT, UPS - Toulouse, France

ARTICLE INFO

Keywords:
Liquid film thickness
Waves
Annular flow
Condensation
Minichannel

ABSTRACT

In the present study, liquid film thickness measurements are performed during vertical downflow condensation inside a 3.38 mm inner diameter channel at 40 °C saturation temperature. Condensation tests are carried out with HFE-7000 in two different test apparatuses, the first being composed of two counter-flow tube-in-tube heat exchangers separated by an adiabatic borosilicate glass tube for flow visualizations and liquid film thickness measurement, while the second consisting of a diabatic sapphire tube coupled with an infrared camera for simultaneous local heat flux and film thickness measurements at low mass flux (5–30 kg m^{-2} s^{-1}). Chromatic confocal imaging and shadowgraphy are applied to the adiabatic borosilicate glass tube for evaluating the liquid film thickness with high temporal and spatial resolution, while punctual optical sensors (chromatic confocal and interferometer) are used in the diabatic sapphire test section. The liquid film thickness results obtained in the two independent laboratories are compared at the same operating conditions, showing an excellent agreement. The effect of mass flux (from 50 to 150 kg m^{-2} s^{-1}) and vapor quality on the liquid film thickness and interfacial waviness of HFE-7000 is discussed by means of both statistical and spectral analyses. The liquid film thickness data of HFE-7000 are compared with those of R245fa and R134a taken during previous experimental campaigns. HFE-7000 generally displays lower film thickness values compared to R245fa and R134a due to the smaller vapor density. At low mass flux (50 kg m^{-2} s^{-1}), such comparison shows the effect of the small liquid viscosity on the thinning of the liquid film in the case of R134a. The accuracy of well-known models for the prediction of the mean film thickness is assessed with comparison to the experimental data of HFE-7000.

1. Introduction

Annular two-phase flow is one of the most frequently encountered flow regimes in practical applications, such as refrigeration and air conditioning systems, steam generators, nuclear and chemical reactors [2]. In annular flows, the liquid phase flows as a continuous film close to the channel wall, while the vapor/gas phase occupies the central core of the channel cross-section. In addition, gas/vapor bubbles can be entrained in the liquid film, as well as liquid droplets in the gas/vapor core [3]. In the case of downward annular flow, a thin "falling film" of liquid is formed in the inner surface of the tube wall even at zero gas/vapor velocity.

Over the years, downward annular flows have been analysed based on the geometrical or topological characterization of the features at the liquid–vapor interface [4–8]. Two main classes of waves are typically identified: (i) "ripple" waves, which display short lifetime and small amplitude, and (ii) "disturbance" waves, which carry a significant portion of the condensate and show amplitudes which are many times higher than the mean film thickness (typically with a factor of 5) [9]. Compared to ripples, disturbance waves travel at much higher velocities, display much longer lifetime and dominate the interfacial mass, momentum and energy transfer [10,11]. Indeed, the development of disturbance waves during annular flow promotes the onset of turbulent eddies beneath the wave crests, hence increasing the heat and mass transfer [12].

A parameter of great importance in two-phase annular flows is the liquid film thickness. The main thermal resistance to heat transfer during annular two-phase flow is related to thermal conduction through the condensate film, which strictly depends on the thickness of the film itself [13]. The film thickness also affects the characteristics of the disturbance waves, the entrainment ratio of liquid droplets and the overall

* Corresponding author.
E-mail address: davide.delcol@unipd.it (D. Del Col).

https://doi.org/10.1016/j.expthermflusci.2023.110963
Received 28 February 2023; Received in revised form 2 May 2023; Accepted 20 May 2023
Available online 25 May 2023

Nomenclature

c	Specific heat [J kg^{-1} K^{-1}]
d	Diameter [m]
e	Percent deviation [%], $= [(\psi_{calc} - \psi_{meas})/\psi_{meas}] \cdot 100$
e_{AB}	Mean absolute deviation [%], $= (1/N_p)\sum(\lvert\psi_{calc} - \psi_{meas}\rvert/\psi_{meas}) \cdot 100$
e_R	Average deviation [%], $= (1/N_p)\sum[(\psi_{calc} - \psi_{meas})/\psi_{meas}] \cdot 100$
f_w	Wave frequency [Hz]
f	Friction factor [-]
g	Gravity acceleration [m s^{-2}]
G	Mass flux [kg m^{-2} s^{-1}]
h	Specific enthalpy [J kg^{-1}]
h_{LG}	Latent heat [kJ kg^{-1}]
HTC	Heat transfer coefficient [W m^{-2} K^{-1}]
j_G	Vapor superficial velocity [m s^{-1}], $= G \cdot x/\rho_V$
j_L	Liquid superficial velocity [m s^{-1}], $= G \cdot (1-x)/\rho_L$
k	Coverage factor [-]
$\dot{m}$	Mass flow rate [kg s^{-1}]
N_p	Number of experimental data points [-]
p	Pressure [bar]
q	Heat flow rate [W]
q'	Heat flux [W m^{-2}]
Ra	Internal surface roughness, defined by ISO 4287:2009 [1] [μm]
Re_F	Reynolds number of the liquid film [-], $= G \cdot (1-x) \cdot (1-\varepsilon) \cdot d/\mu_L$
Re_G	Reynolds number of the vapor phase [-], $= G \cdot x \cdot d/\mu_G$
Re_L	Reynolds number of the liquid phase [-], $= G \cdot (1-x) \cdot d/\mu_L$
Re_{LO}	Liquid-only Reynolds number [-], $= G \cdot d/\mu_L$
T	Temperature [°C]
u	Standard uncertainty.
x	Thermodynamic vapor quality [-]
z	Axial position [m]

Greek letters

ε	Entrained liquid fraction [-]
δ	Liquid film thickness [μm]
δ^+	Dimensionless liquid film thickness [-]
Δp	Pressure difference [kPa]
ΔT	Temperature difference [K]
λ	Thermal conductivity [W m^{-1} K^{-1}]
μ	Dynamic viscosity [kg m^{-1} s^{-1}]
τ_{wall}	Wall shear stress [Pa]
ρ	Density [kg m^{-3}]
σ	Surface tension [N m^{-1}]
σ_N	Standard deviation [%], $= \left\{\left[\sum(e - e_R)^2\right]/(N_p - 1)\right\}^{1/2}$
Φ_{LO}	Two-phase frictional pressure drop multiplier [-]

Subscripts

air	Air
base	Base film thickness
calc	Calculated
e	External
F	Liquid film
G	Vapor
i	Internal
in	Inlet
L	Liquid
LO	Liquid-only
mean	Mean
meas	Measured
out	Outlet
red	Reduced
ref	Refrigerant
sat	Saturation
wall	Wall
water	Water

pressure drop [14]. Therefore, the fundamental understanding of liquid film and disturbance waves characteristics is necessary for the accurate prediction of the system behaviour in annular flow.

Due to the complexity of the annular flow mechanisms, various experimental techniques have been used to characterize the flow properties during annular two-phase flow. For large diameter tubes (inner diameter higher than 10 mm), the instrumentation methods for film thickness measurement typically include conductance probes [15,16], ultrasound [17], fluorescence techniques [18–20] and high-speed video imaging [21].

When moving to mini-/micro-channels, the characterization of the film thickness and interfacial features becomes even more complex since the measurement technique must be extremely precise as the liquid film is generally thin (about 10–100 μm). Moreover, non-intrusive measuring techniques are required to avoid disturbance of the flow. Thanks to the development of visual/optical techniques and digital image processing technology, optical methods have shown great advantages in studying liquid–vapor flows at micro-scale since they are easy to be implemented and non-intrusive, leading to reasonable measuring accuracy [22–24]. Han et al. [25,26] experimentally evaluated the liquid film thickness of ethanol inside parallel channels with height of 0.1, 0.3 and 0.5 mm by means of an interferometer and a laser focus displacement meter (LFDM). Donniacuo et al. [27] developed an optical method based on the detection of the liquid–vapor interface from high-speed camera images for measuring the top and bottom liquid film thickness of R245fa during annular flow in a 2.95 mm horizontal circular channel. Recently, Zhang et al. [28] measured the liquid film thicknesses of R245fa and zeotropic mixtures of R134a/R245fa during flow condensation inside a circular micro-channel with 1 mm inner diameter using a CCD camera and a laser focus displacement meter (LFDM). Berto et al. [29,30] performed film thickness measurements with R245fa and R134a during vertical downflow condensation inside a 3.38 mm inner diameter pipe by means of combined shadowgraph technique (applied to a sequence of flow pattern images recorded by a high-speed camera) and chromatic confocal imaging. Beaumale et al. [31] experimentally obtained the axial profiles of liquid film thickness during vertical downflow condensation of HFE-7000 at mass fluxes below 30 kg m^{-2} s^{-1} inside a 3.38 mm inner diameter sapphire tube by using a white light interferometer and a chromatic confocal sensor.

From the literature review, it emerges that limited quantitative data of local and instantaneous film thickness inside minichannels are available. Extended databases covering a wide range of operating conditions are needed for the development/assessment of correlations and for the validation of computational fluid dynamics simulations [32].

In the present study, liquid film thickness measurements are performed with HFE-7000 during vertical downflow condensation inside a 3.38 mm inner diameter channel at 40 °C saturation temperature. Two different test rigs, respectively located in Padova (Italy) and in Toulouse (France), have been used: the first consists of two counter-flow tube-in-tube heat exchangers separated by an adiabatic borosilicate glass tube for film thickness measurement; the second is made of a diabatic sapphire tube. Chromatic confocal imaging and shadowgraphy are applied to the adiabatic borosilicate glass tube, while punctual optical sensors (chromatic confocal and interferometer) are used in the diabatic sapphire test section.

The present paper is aimed at:

- showing that the liquid film thickness during vertical downflow condensation can be measured either using a short adiabatic visualization window or performing measurements directly in a diabatic test section;
- providing more experimental film thickness data with HFE-7000 inside minichannels;
- studying the effect of fluid properties on film thickness and waves characteristics;
- assessing available correlations for film thickness prediction.

2. Experimental apparatuses and data reduction

In the present paper, liquid film thickness data of HFE-7000 obtained in two independent setups are compared at the same working conditions with the aim of checking the agreement between the experimental datasets taken using two different techniques. The two experimental setups are respectively located at the Laboratory of Two-Phase Heat Transfer of the Department of Industrial Engineering of the University of Padova (Italy) and at Laboratory on Plasma and Conversion of Energy (LAPLACE) of Université Paul Sabatier in Toulouse (France). In both cases, the condensation heat transfer test section displays an inner diameter of 3.38 mm and is designed to allow the simultaneous measurement of liquid film thickness and heat transfer coefficients. In the experimental device located in Padova (Italy), the film thickness measurements, together with flow pattern visualizations, are performed in an adiabatic glass window, where the working fluid flows at the desired thermodynamic conditions (set in a previous heat exchanger in which the condensation heat flow rate is removed by using cooled water). Instead, the film thickness measurements performed in Toulouse (France) are conducted in a diabatic test section in sapphire, where the refrigerant condenses inside the tube and the heat flow rate is removed by cold air flowing on the external side. Due to the different thermodynamic and transport properties of the secondary fluids (water and air), the achieved heat fluxes in the two experimental test sections are different. Indeed, if considering HFE-7000 as working fluid, at mass velocities equal to 20 and 30 kg m^{-2} s^{-1} the heat fluxes are in the range 2.9–3.6 kW m^{-2} for the experimental setup in Toulouse, while varying between 4.4 and 6.9 kW m^{-2} for the test section employed in Padova. A maximum mass flux of HFE-7000 equal to $G = 30$ kg m^{-2} s^{-1} can be realized in the experimental apparatus in Toulouse (France) to condense all the vapor, while a wider range of mass fluxes (from 20 to about 250 kg m^{-2} s^{-1}) can be tested in Padova (Italy). More details about the employed test sections and the optical setup are presented in the next sections.

It is important to stress that, in the present work, the liquid film thickness measurements are performed along the tube length and not crosswise at different circumferential positions, since a 3D experiment would clearly increase the complexity of the apparatus. Therefore, waves are assumed to present similar characteristics regardless the chosen circumferential position, in accordance with the experimental findings of Fershtman et al. [33] during annular two-phase flow inside a 24 mm inner diameter vertical tube.

2.1. *Experimental setup at the Laboratory of Two-Phase Heat Transfer in Padova (Italy)*

The experimental setup used for condensation tests in Padova (Italy) allows to measure the liquid film thickness in a dedicated glass window with high spatial and temporal resolution, together with quasi-local heat transfer coefficient measurements. It is composed of a primary refrigerant loop and three auxiliary water circuits. Before entering the condensation test section, the subcooled refrigerant is vaporized and superheated in a tube-in-tube heat exchanger.

The test section for film thickness measurements and flow visualizations, which was already presented in previous works [29,34,35], consists of a 40 mm long borosilicate glass tube interposed between two counter-flow tube-in-tube heat exchangers, being respectively 540 mm and 480 mm long. Each heat exchanger is divided in three and two subsectors: the refrigerant flows in the internal channel transferring heat to distilled water, which is employed as secondary fluid. A finned geometry is machined on the water side to augment the heat transfer area and to allow the insertion of wall thermocouples (six thermocouples for each sub-sector). Lexan tubes are used as containment to create the water path.

On the water side, two T-type thermocouples (accuracy $\pm$ 0.05 °C) and a triple-junction thermopile (accuracy $\pm$ 0.03 °C) are used to check the temperature difference of the water between inlet and outlet of each sub-sector. Since the inlet and outlet water temperatures are necessary for the determination of the heat flow rate, helicoidal mixers are placed on the water side before the inlet and after the outlet to get the adiabatic mixing cup temperature. The refrigerant and water mass flow rates are measured by Coriolis mass flow meters (accuracy of $\pm$ 0.14% at 10 kg h^{-1} and $\pm$ 0.2% at 2 kg h^{-1} on the water and refrigerant side, respectively). The refrigerant temperatures at the inlet and outlet of the test section are measured by T-type thermocouples (accuracy $\pm$ 0.05 °C). The inlet pressure is determined by relative pressure transducers (accuracy $\pm$ 5 kPa), while the pressure drop along the test section is evaluated by two differential pressure transducers with different measuring ranges (accuracy $\pm$ 0.12 kPa at $\Delta p > 1$ kPa, accuracy $\pm$ 0.1% at $\Delta p < 1$ kPa).

For each test run, the heat flow rate exchanged on the water side in each *j*-th sector is calculated from a heat balance on the water side:

$$q_{water,j} = \dot{m}_{water,j} \cdot c_{water} \cdot \Delta T_{water,j} \tag{1}$$

where $\dot{m}_{water,j}$ is the water mass flow rate, c_{water} is the water specific heat and $\Delta T_{water,j}$ is the temperature difference between inlet and outlet on the water side (measured by the *j*-th thermopile).

The heat flow rate $q_{water,j}$ is employed to determine the specific enthalpy at the outlet of the *j*-th sector $h_{out,j}$ from the measured refrigerant mass flow rate $\dot{m}_{ref}$ and the inlet enthalpy (for the first sector the inlet enthalpy is evaluated from the measured inlet pressure and temperature):

$$h_{out,j} = h_{in,j} - \frac{q_{water,j}}{\dot{m}_{ref}} \tag{2}$$

The outlet vapour quality in each sub-sector $x_{out,j}$ is determined using the following equation:

$$x_{out,j} = \frac{h_{out,j} - h_L}{h_G - h_L} \tag{3}$$

where h_L and h_G are respectively the liquid and vapor specific enthalpy at saturation pressure. The outlet enthalpy of the *j*-th sector, as well as the outlet vapor quality, corresponds to the inlet enthalpy and vapor quality of the following $(j + 1)$-th sector. The mean vapor quality x in each *j*-th sector is calculated as the average between the inlet and outlet values. The saturation temperature T_{sat} is computed from the measured saturation pressure at inlet/outlet of the test section and using REFPROP 10.0 [36].

The uncertainty analysis has been performed following the JCGM [37] guidelines. Considering the present experimental database, the maximum expanded uncertainty on vapor quality (coverage factor $k = 2$) is equal to $\pm$ 0.017 at $G = 20$ kg m^{-2} s^{-1}. Additional information on the experimental setup and the procedure for data reduction and uncertainty analysis is reported in Azzolin et al. [34].

Before starting the experimental test runs, HFE-7000, which is a low pressure fluid, undergoes a degassing procedure in order to remove non-condensable gases that may be dissolved in the liquid phase. The fluid is heated up and vaporized by means of electric resistors and the resulting mixture of vapor and non-condensable gases migrates to a vacuum cylinder which is cooled down by ice. The non-condensable gases are then sucked and dispersed by a vacuum pump.

2.2. Experimental setup at LAPLACE in Toulouse (France)

The experimental setup located in Toulouse (France) allows the simultaneous measurement of local liquid film thickness and heat transfer coefficient during downward flow condensation at low mass fluxes [38,39].

The test section is placed between two tanks in which the fluid is in liquid–vapor equilibrium state. The pressure inside each tank is set by circulating water at imposed temperature on the external wall. Thus, a constant pressure difference is created between the ends of the test section (Fig. 1). Inside the inlet tank the temperature is set at 60 °C (the corresponding saturation pressure is equal to 2.36 bar), while in the outlet one 40 °C temperature is imposed (the corresponding saturation pressure is equal to 1.25 bar). The vapor flow rate is adjusted using a micrometric valve located between the inlet tank and the entrance of the condenser. It must be stressed that the significant pressure drop inside this micrometric valve (around 1 bar) allows to produce a very stable vapor flow rate as the pressure fluctuations inside the condensation flow are several orders of magnitude smaller compared to this pressure drop. The vapor line between the inlet tank and the test section is heated up by an electrical resistance wrapped around the tube to maintain the vapor in a slightly superheated state until it enters the condenser. The condenser is composed of a vertical sapphire tube of 1 m length with internal and external diameters equal to 3.4 mm and 6 mm, respectively. The transparency of the sapphire in the visible light allows the employment of optical punctual sensors to measure the local liquid film thickness. A white light interferometer and a confocal sensor are used, which can be moved along the axial direction of the tube by a translation stage to determine the local temporal evolution of the liquid film thickness all along the tube.

The external wall of the sapphire tube is cooled down by air whose temperature is controlled by an air-conditioning system. An IR camera (FLIR® SC6000HS) and a reference black surface are fixed on the same translation stage than the optical sensors in order to determine the external wall temperature profile along the tube simultaneously with the

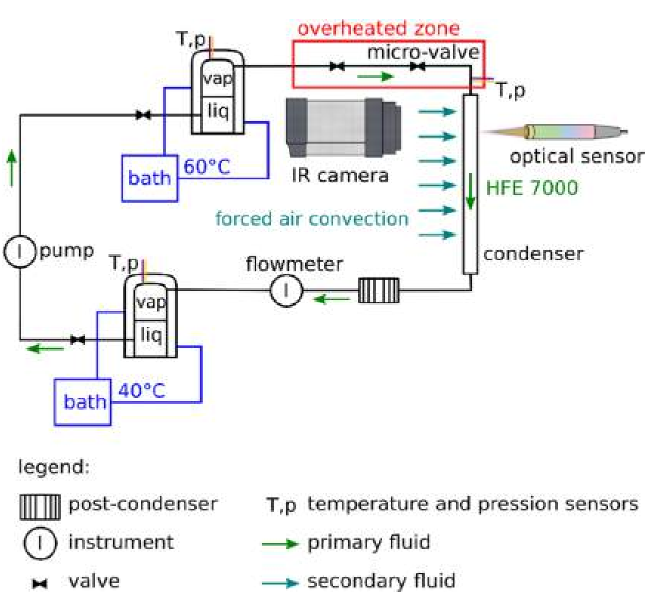

Fig. 1. Schematic of experimental setup employed at LAPLACE, Université Paul Sabatier in Toulouse (France).

film thickness one. Between the exit of the sapphire tube and the outlet tank, a post-condenser is employed to ensure the complete condensation of the vapor before entering a Coriolis mass flowmeter (±0.2% accuracy). Depending on the duration of each experiment, a mechanical pump is used to transfer part of the liquid contained in the outlet tank towards the inlet one which may be empty after several test runs.

K-type thermocouples are used with EC-kind compensation (±0.2 °C accuracy) for air temperature measurements close to the condenser and HA-kind (±0.05 °C accuracy) for tanks and condenser measurements. Each tank is instrumented with a pressure sensor (accuracy of ± 2.8 mbar and ± 20 mbar for the inlet and outlet tanks, respectively). Another pressure sensor is positioned upstream from the condenser inlet (±1.6 mbar accuracy) and its readings are used to determine the saturation temperature within the condenser. The correspondence between saturation temperature and pressure readings has been previously calibrated in-situ leading to an uncertainty of ± 0.058 °C. Pressure and temperature data are monitored at a frequency of 1 Hz using Keysight and Agilent 34970A acquisition devices.

The condensation heat flux is deduced from the knowledge of the external wall temperature given by the infrared camera [31]. Since the external heat transfer coefficient induced by the air cooling (around 80 W m^{-2} K^{-1}) is small as compared to the one obtained during condensation process (several hundreds of W m^{-2} K^{-1}), a low saturation-to-wall temperature difference would adversely affect the determination of the condensation heat transfer coefficient. Therefore, a specific differential IR technique was developed with the aim to increase the accuracy of the wall temperature measurement. First, as the sapphire is not completely opaque in the detection wavelengths range of the IR camera (3 to 5 μm), a thin layer line of black paint was deposited along the external wall of the condenser. Even if the reflectivity of the paint is very low (<5%), small variations of the IR ambient reflections and errors induced by the auto-correction of the offset of the camera with ambient temperature in the Non Uniformity Corrections (NUC) procedure (of the pixels) can lead to biases of around 0.4 °C. To correct these biases, a reference surface, whose temperature is precisely known, is provided with the same black paint used for the sapphire tube. This reference surface and the tube black paint are then visualized simultaneously thanks to a set of mirrors. The difference between the infrared signals coming from the tube paint and the reference surface was then calibrated with the corresponding temperature difference. With this procedure, measurement of the wall temperature with the IR camera becomes independent of the ambient fluctuations. The precision using this kind of calibration allows to reach 0.04 °C of repeatability (instead of 0.4 °C without using the reference surface).

To obtain the heat transfer coefficient between the external wall of the sapphire tube and the air flow, a dedicated calibration is first realized considering a water flow inside the test section. The water flow was adjusted to obtain a temperature difference between inlet and outlet within 10–20 °C with a water inlet temperature varying from 42 to 50 °C during the experiments. The first three experiments were conducted with $T_{air} = 22$ °C, while the others with $T_{air} = 11$ °C. The wall temperature profiles along the tube axis were recorded for each experiment using the IR calibration curve. The external heat transfer coefficient was deduced by:

$$\mathrm{HTC}_e = \frac{q' \cdot \frac{d_i}{d_e}}{T_{wall,e} - T_{air}} \tag{4}$$

where q' is the local heat flux deduced from Eq. (5), d_i and d_e are respectively the internal and external diameters of the sapphire tube, $T_{wall,e}$ is temperature of the black paint on the outer wall and T_{air} is the air temperature.

$$\frac{\mathrm{d}q'}{\mathrm{d}z} = q' \cdot \left(\frac{\mathrm{dHTC}_i}{\mathrm{d}z} \cdot \frac{1}{\mathrm{HTC}_i} - \frac{\pi \cdot d_i \cdot \mathrm{HTC}_i}{\dot{m} \cdot c_L} \right) - \mathrm{HTC}_i \cdot \frac{\mathrm{d}T_{wall,i}}{\mathrm{d}z} \tag{5}$$

In Eq. (5), HTC_i is the internal heat transfer coefficient, evaluated using the Shah and London [40] correlation in laminar regime, $\dot{m}$ is the water mass flow rate, c_L is the water specific heat and $T_{wall,i}$ is the internal wall temperature, deduced from the outer one and from the paint and sapphire thermal resistances.

The external heat transfer coefficients obtained for the six experiments (each being at a different water inlet temperature) were found to be within 70–90 W m^{-2} K^{-1}.

The local vapor quality x can be then obtained from an enthalpy balance:

$$x(z) = 1 - \frac{4 \cdot d_e}{d_i^2 \cdot G \cdot h_{LG}} \cdot \int_0^z \text{HTC}_e(\xi) \cdot \left[T_{wall,e}(\xi) - T_{air}\right] \cdot d\xi \quad (6)$$

where G is the mass flux, h_{LG} is the latent heat of vaporization and the origin of the abscissa ($z = 0$) corresponds to the beginning of the condensation.

When considering the whole length of the condensation zone, Eq. (6) leads to a maximum error on the vapor quality value of<2% whatever the mass flux considered.

3. Optical setups for film thickness measurements

3.1. Optical setup at the Laboratory of Two-Phase Heat Transfer in Padova (Italy)

The optical setup employed in Padova (Italy) allows the measurement of the liquid film thickness with two complementary techniques and the acquisition of flow pattern visualizations. As shown in Fig. 2, it consists of a high-speed camera, a LED light source, a borosilicate glass tube (located between the two tube-in-tube heat exchangers) and a chromatic confocal sensor. Such optical setup was used in previous experimental investigations [30,41].

Flow visualizations are acquired by means of a high-speed camera (Photron® FASTCAM Mini UX100), together with a Navitar® Zoom 7000 18–108 mm macro lens and a LED light source. The camera and the LED source are located facing each other with the glass tube placed in the middle. The LED source can be considered as a parallel light emitter from the camera point of view, due to the great distance between the light source and the glass window (around 70 cm). The image size is set to 1024 pixels (height) by 896 pixels (length) and the resolution of the camera is equal to 10.9 μm/pixel.

The borosilicate glass tube, having an inner diameter equal to 3.38 mm, is designed with two symmetric curved parts and two parallel flat sides. The special curvature of the glass tube allows to magnify the liquid film thickness observed by the high-speed camera, whereas the two flat

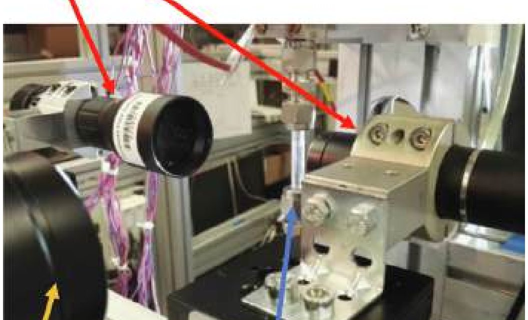

Fig. 2. Optical setup at University of Padova consisting of a glass tube, a high-speed camera, a LED light source and optical sensors (a chromatic confocal sensor and an interferometer).

parts (2.85 × 15 mm in the axial direction) are designed to avoid defocus of incident light and enable the employment of punctual optical sensors, such as the chromatic confocal sensor.

The liquid film thickness inside the channel is determined by combining the shadowgraph technique, applied to the fluid flow images acquired by the high-speed camera, and the local measurements performed by the chromatic confocal sensor. With the shadowgraph technique, the recorded RGB images are first binarized by choosing manually the proper threshold value to allow an accurate interface detection [30]. A ray-tracing method (extended version of the one presented by Médéric et al. [42] to non-cylindrical surfaces) is then applied to correct the liquid film thickness determined from the images accounting for the optical distortions induced by the specific shape of the glass tube.

The chromatic confocal sensor employed in the present setup is the same used in LAPLACE Laboratory, with a maximum measurable film thickness value of 300 μm. During the experiments, the chromatic confocal sensor is synchronized with the high-speed camera at 1000 Hz frequency to allow simultaneous liquid film thickness measurements and flow visualizations. Thanks to the synchronization of the chromatic confocal sensor with the high-speed camera, it is possible to obtain an in-situ calibration curve in the measuring range of the punctual sensor that links the apparent liquid film thickness (in pixels) resulting from the shadowgraph technique to the real liquid film thickness (in microns) measured by the confocal sensor. The calibration curve effectively considered in the present work for the evaluation of the actual liquid film thickness results from the combination of the aforementioned in-situ calibration curve (up to 300 μm) and the theoretical calibration curve calculated from the ray-tracing model. Liquid film thickness values below 20 μm cannot be directly determined with the shadowgraph technique due to the spatial resolution of the camera. Such measuring shortcoming can be compensated by the simultaneous chromatic confocal measurements at the sensor position, with minimum measured liquid film thickness values of 2–3 μm. More details regarding the optical system and the employed techniques are reported in Berto et al. [29].

The uncertainty values on the liquid film thickness measured by the confocal sensor and with the shadowgraph technique are evaluated following the procedure reported in Berto et al. [29].

The expanded (coverage factor $k = 2$) standard uncertainty of the film thickness is ± 2 μm in the case of the confocal sensor, while it varies between ± 10 μm and ± 15 μm when using the shadowgraph technique.

3.2. Optical setup at LAPLACE Laboratory in Toulouse (France)

The measurement of the liquid film thickness is realized using two different sensors: a confocal chromatic sensor and an interferometric sensor. Both of them allow the determination of the liquid film thickness from the analysis of backscattered light in the visible spectrum reflected by both the inner wall and liquid–vapor interface. In order to avoid the defocus of light induced by the cylindrical surface of the external wall, a flat surface of 3 mm width, having the same optical index of sapphire, was realized over the entire length of the tube. The spectrometer of the STIL-DUO (STIL®) apparatus is used to characterize the optical signal coming from the two sensors and then to deduce the liquid film thickness. At the entrance of the sapphire tube the liquid film is thin (from 0 μm to 50 μm) and the amplitude of the wave is low compared to the mean liquid film thickness. In such situation the interferometer is well suited and allows to determine the temporal evolution of the film thickness at 2000 Hz with a precision of 10 nm. At higher axial distance from the tube entrance, the amplitude of the waves is increased, the local slope of the interface is higher and the maximum liquid film thickness at one axial position is often greater than 50 μm. In that case the chromatic confocal sensor can be suitably used to detect the temporal evolution of the liquid film thickness. The STIL® CL2MG70 confocal sensor pen is able to measure liquid film thickness values up to

300 μm with slope of the liquid–vapor interface up to 28°. The temporal evolution of the liquid film is determined at 400 Hz by the chromatic confocal sensor, with an uncertainty on each measurement point around 1 μm mainly due to the broadening of the intensity of the peak corresponding to the position of the liquid–vapor interface in the spectrum, created by the rapid change in the thickness of the liquid film during the exposure time (1/400 s).

4. Experimental results

In the present section, the film thickness values of HFE-7000 measured during condensation under vertical downflow are reported at 40 °C saturation temperature inside the 3.38 mm inner diameter channel. Experimental tests were conducted at the Laboratory of Two-Phase Heat Transfer in Padova (Italy) at mass flux ranging from 20 to 150 kg m^{-2} s^{-1} and at different vapor quality. The film thickness results at mass flux $G = 20$ kg m^{-2} s^{-1} and $G = 30$ kg m^{-2} s^{-1} are compared with those obtained in the experimental setup located in Toulouse (France). In Table 1 the working conditions during the condensation tests of HFE-7000 in the two independent experimental setups are summarized.

With regard to the experimental tests performed in Padova (Italy), the superheating of the vapor at the inlet of the test section is kept equal to 15–17 K. The first sub-sector of the condensation test section is employed to cool down the superheated vapor and set the desired thermodynamic state at the inlet of the second sub-sector. Hence, the corresponding mean vapor quality is discarded. In order to simultaneously perform flow visualizations and film thickness measurements at different operating conditions, the vapor quality at the inlet of the glass tube is varied by changing the condensation rate in the first heat exchanger. The change of vapor quality between the outlet of the first heat exchanger and the inlet of the second one can be neglected due to the low heat transfer coefficient on the external side of the glass tube and its small length [29].

Instead, in the experimental setup located in Toulouse (France), local vapor qualities and local film thickness values are measured. During the tests, the superheating of the vapor at the inlet of the test section is kept in the range 7–7.5 K.

4.1. Comparison between the two experimental datasets

Fig. 3 reports the comparison between the mean liquid film thickness obtained in the two independent experimental setups at $G = 20$ kg m^{-2} s^{-1} and $G = 30$ kg m^{-2} s^{-1} as function of the vapor quality. Such values are intended as the average of all the instantaneous film thickness values measured during the acquisition time (equal to 3.1 s for the experimental tests in Padova and to 10 s for those performed in Toulouse). The acquisition frequency is set to 1000 Hz and 400 Hz for the tests in Padova and in Toulouse, respectively. The interpolation curve obtained from the measurements performed in Toulouse (France) is also plotted to better follow the evolution of the average thickness as a function of vapor quality. As shown in Fig. 3, in the experimental setup used in Padova the film thickness values at $G = 20$–30 kg m^{-2} s^{-1} are measured only at small vapor quality since in the first heat exchanger, before the glass tube, the superheated vapor was almost fully condensed to allow heat flow rate and vapor quality measurements with low uncertainty.

Fig. 3 shows that very similar film thickness values are obtained in the two experimental test benches. Moreover, it is interesting to note that the film thickness measurements conducted in Padova (Italy) involve an adiabatic glass section placed between two diabatic parts, while in Toulouse (France) liquid film thickness measurements are directly performed in a diabatic tube where the phase change is present. Notwithstanding the smaller heat flow rates obtained with Toulouse setup and the different experimental procedures, no deviations between the two experimental databases can be observed.

In order to carry out a fair comparison between the two experimental datasets, a statistical and spectral analysis of the instantaneous liquid film thickness data is also performed. Indeed, even if the mean liquid film thickness is the same for both cases, the amplitude and frequency of the interfacial waves could be different. In Fig. 4 the probability density function (PDF) of liquid film thickness values of HFE-7000, measured in the two different experimental setups, at mass flux equal to 20 kg m^{-2} s^{-1} and vapor quality $x = 0.08$–0.10 and $x = 0.31$ are reported. The same comparison is reported in Fig. 5 at mass flux equal to 30 kg m^{-2} s^{-1} and vapor quality $x = 0.27$ and $x = 0.55$. The PDFs are calculated considering about 3100 and 4000 instantaneous film thickness values for Padova and Toulouse datasets, respectively, recorded during the acquisition time. An interval for each class equal to 10 μm is chosen for the calculation of the PDF.

At $G = 20$ kg m^{-2} s^{-1} (Fig. 4) no significant difference between the PDFs obtained in Padova and in Toulouse can be observed. The range of detected film thickness values is comparable in the two cases, as well as the most probable film thickness value (between 60 and 70 μm for $x = 0.08$–0.1, between 50 and 60 μm for $x = 0.31$). As expected, the peak film thickness is observed at smaller values with the increasing vapor quality. As already shown in Fig. 3, the deviation between mean film thickness values in the two experimental setups is small (+2% at $x = 0.08$–0.1, −2% at $x = 0.31$ comparing data taken in Toulouse to those of Padova).

The same can be argued also for $G = 30$ kg m^{-2} s^{-1}, as shown in Fig. 5. The PDFs of liquid film thickness data taken in Toulouse and in Padova display similar shapes for both the considered vapor quality values ($x = 0.27$ and $x = 0.55$). The deviation between the mean film thickness values measured in Toulouse and in Padova never exceeds 3% for the considered working conditions. The calculated δ_{mean} value does not represent the most probable film thickness in the PDFs at $G = 20$ kg m^{-2} s^{-1} and $G = 30$ kg m^{-2} s^{-1}.

It can be observed that, as the liquid film thickness increases, the PDF obtained in Toulouse decreases more smoothly compared to the other PDF. Indeed, there are some small differences in the film thickness trends measured in the two experimental setups which, however, do not influence the mean characteristics of the liquid film. This PDF difference can be due to several reasons, such as the different acquisition frequency (1000 Hz in Padova, 400 Hz in Toulouse) or the effect of the heat flux on the film thickness evolution. In the experimental setup located in Toulouse the condensation process occurs continuously inside the sapphire channel under almost uniform heat flux (in the range 2.9–3.6 kW m^{-2}), leading to less abrupt changes in the liquid film thickness evolution; in Padova test rig the liquid film forms in the diabatic copper part of the test section and is measured in the following adiabatic glass window, after the first heat exchanger (displaying 4.4–6.9 kW m^{-2} at $G = 20$–30 kg m^{-2} s^{-1}). This latter configuration may be responsible for the observed differences in the PDFs.

In order to complete the present comparative analysis, the power spectral density (PSD) in the frequency domain of the liquid film thickness records obtained in the two independent setups is calculated. The PSDs are obtained averaging the results of the Welch algorithm,

Table 1
Working conditions during the condensation tests with HFE-7000 (the values between brackets correspond to the maximum variation with respect to the set value).

Experimental setup	p_{sat} [bar]	G [kg m^{-2} s^{-1}]	x [-]
Padova	1.25 (-0.05, +0.07)	20 (-2.5%, +1.8%)	0.1–0.31
		30 (-1.2%, +1.2%)	0.16–0.55
		40 (-2.1%, +2%)	0.21–0.71
		50 (-1.3%, +2.2%)	0.19–0.78
		60 (-1.6%, +1.5%)	0.19–0.75
		70 (-1.9%, +0.3%)	0.21–0.76
		80 (-0.3%, +1.4%)	0.22–0.77
		100 (-0.4%, +0.7%)	0.23–0.78
		150 (-1.4%, +2.7%)	0.21–0.61
Toulouse	1.25 (-0.01, +0.02)	20 (-1.2%)	0.03–1
		30 (-1.6%)	0.15–1

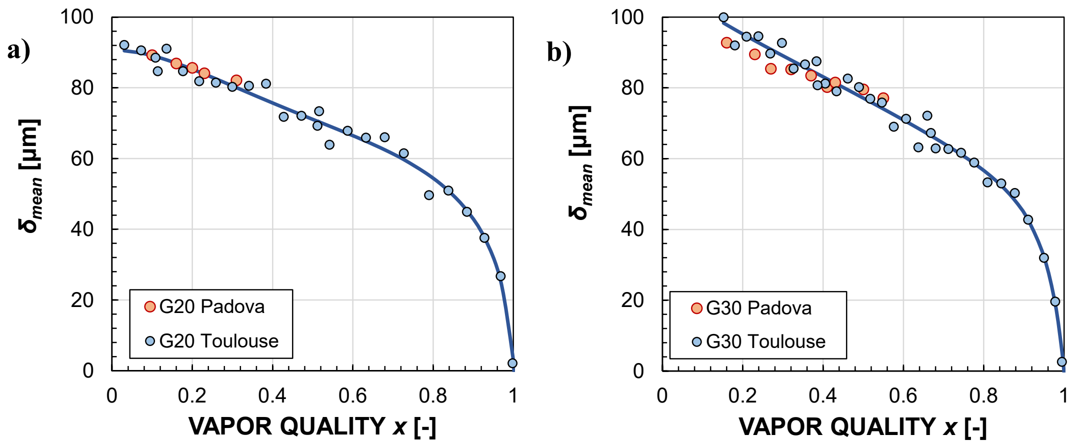

Fig. 3. Experimental mean liquid film thickness δ_{mean} of HFE-7000 at 40 °C saturation temperature versus vapor quality, measured in the two experimental setups in Toulouse (France) and in Padova (Italy): comparison at a) mass flux $G = 20$ kg m^{-2} s^{-1} and b) at $G = 30$ kg m^{-2} s^{-1}.

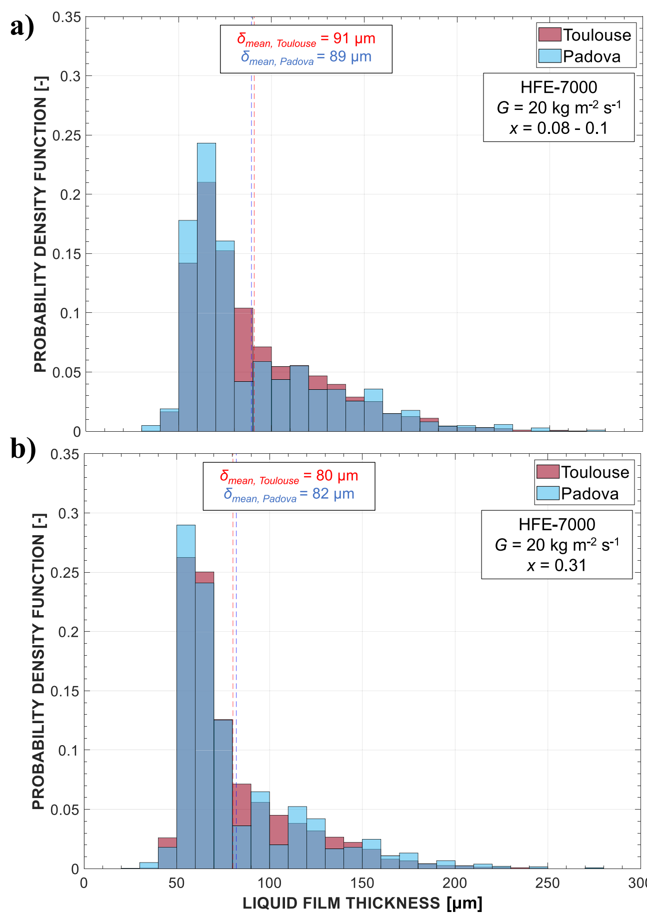

Fig. 4. Comparison between the probability density functions (PDFs) of liquid film thickness of HFE-7000 measured with the experimental setups located in Toulouse (France) and in Padova (Italy) at mass flux $G = 20$ kg m^{-2} s^{-1}: a) vapor quality $x = 0.08$–0.1; b) vapor quality $x = 0.31$. The mean film thickness values are also reported in the histograms. The dark blue region corresponds to the superposition of the two PDFs. (For interpretation of the references to colour in this figure legend, the reader is referred to the web version of this article.)

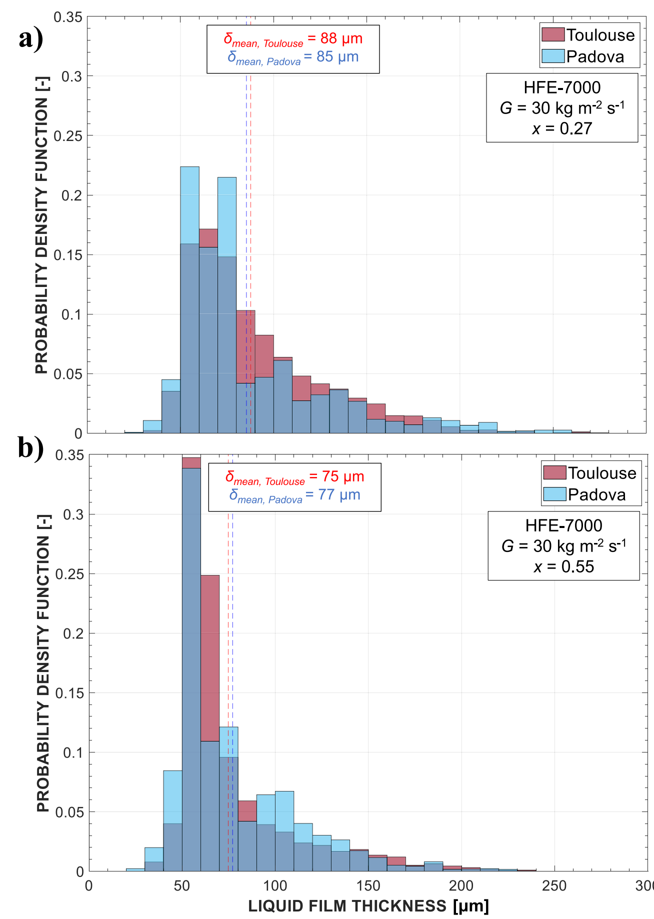

Fig. 5. Comparison between the probability density functions (PDFs) of liquid film thickness of HFE-7000 measured with the experimental setups located in Toulouse (France) and in Padova (Italy) at mass flux $G = 30$ kg m^{-2} s^{-1}: a) vapor quality $x = 0.27$; b) vapor quality $x = 0.55$. The mean film thickness values are also reported in the histograms. The dark blue region corresponds to the superposition of the two PDFs. (For interpretation of the references to colour in this figure legend, the reader is referred to the web version of this article.)

using a Hamming window of length equal to 1024 samples and with 50% overlap. Each liquid film thickness time series acquired in Padova and in Toulouse consists of about 3110 and 4000 points, respectively (the corresponding acquisition frequency is equal to 1000 Hz and 400 Hz). Figs. 6 and 7 respectively show the PSDs of wave frequency of HFE-7000 at mass flux equal to 20 and 30 kg m^{-2} s^{-1} and at different vapor quality values. For both mass fluxes, the PSDs obtained considering the two independent experimental databases display similar shape, with the

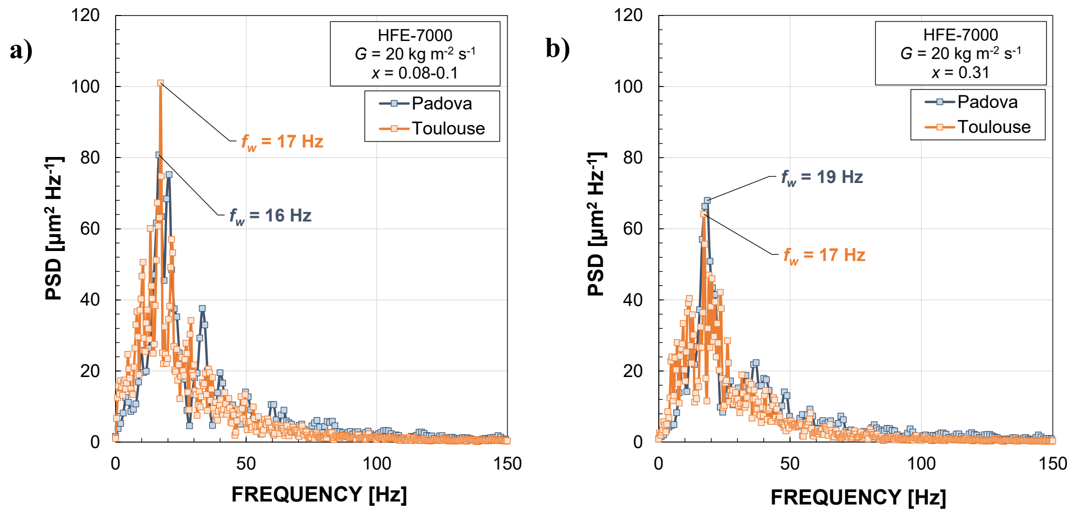

Fig. 6. Comparison between the experimental datasets taken in Padova (Italy) and in Toulouse (France) in terms of power spectral density (PSD) of wave frequency for fluid HFE-7000 at mass flux $G = 20$ kg m^{-2} s^{-1}: a) vapor quality $x = 0.08$–0.10, b) vapor quality $x = 0.31$.

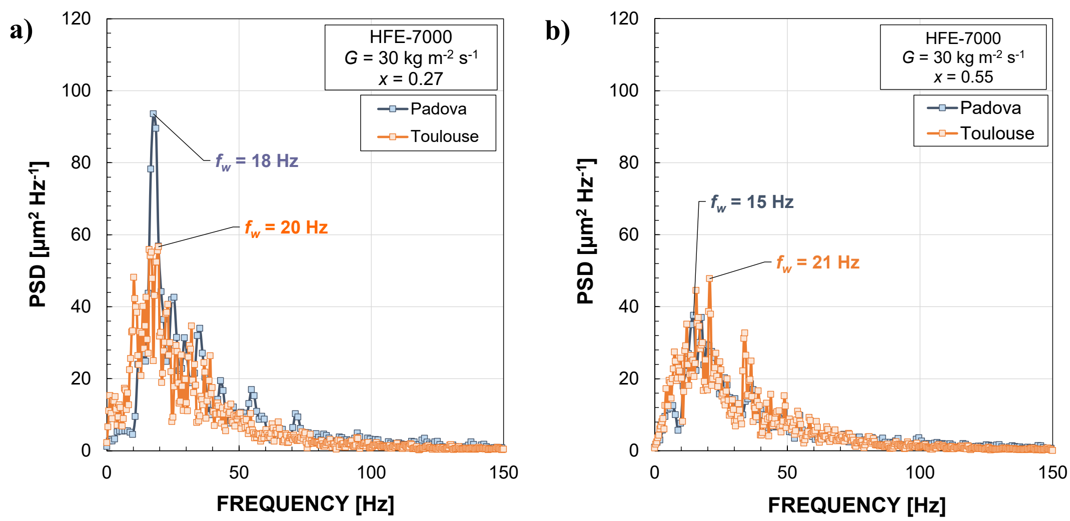

Fig. 7. Comparison between the experimental datasets taken in Padova and in Toulouse in terms of power spectral density (PSD) of wave frequency for fluid HFE-7000 at mass flux $G = 30$ kg m^{-2} s^{-1}: a) vapor quality $x = 0.27$, b) vapor quality $x = 0.55$.

PSD peak encountered at almost identical frequency (at 15–20 Hz). Comparing Figs. 6a) and 6b), as well as Figs. 7a) and 7b), the PSD peak amplitude reduces with the increasing vapor quality due to the smaller waves height, while the main frequency slightly increases.

To conclude, the coherence between the two independent databases in terms of statistical and spectral characteristics confirms the compatibility of the results: both the techniques (one using an adiabatic sector placed between two diabatic sectors in which the condensation is promoted by water, the other using a sapphire tube cooled by external air) can be used for the measurement of the liquid film thickness during in-tube annular condensation. Moreover, from the comparison it emerges that the measured liquid film thickness values at the same vapor quality and mass flux during condensation in vertical downflow basically do not depend on the heat transfer process, but only on hydrodynamics, at least for the present operating conditions (for example, heat flux range).

4.2. Flow pattern visualizations

Fig. 8 shows flow visualizations of HFE-7000 during condensation in vertical downflow at varying mass flux (from 30 to 150 kg m^{-2} s^{-1}) and vapor quality. Such flow visualizations are acquired during condensation tests at the Laboratory of Two-Phase Heat Transfer of the University of Padova (Italy). The liquid phase at the tube wall can be distinguished as the clearer zones at the top and at the bottom of the images, while the vapor flow correspond to the darker region around the tube axis. The white central region is related to light rays reaching the glass tube surface with an incident angle close to the normal.

Annular flow is detected for all the operating conditions. At $G = 30$ kg m^{-2} s^{-1} and $G = 50$ kg m^{-2} s^{-1} no significant differences in terms of interfacial waviness can be observed. The liquid–vapor interface is weakly rippled at low vapor quality, while interfacial waves display higher frequency and smaller height with the increasing vapor quality. At $G = 70$ kg m^{-2} s^{-1} high-amplitude interfacial instabilities are first detected at $x = 0.21$, displaying long wavelength, and even at higher vapor quality values ($x = 0.56$) but with smaller wavelength. Such waves supposedly act for thinning the liquid film, which indeed appears smaller at $G = 70$ kg m^{-2} s^{-1} compared to lower mass fluxes. At $G = 80$ kg m^{-2} s^{-1} interfacial disturbance waves are observed at $x = 0.22$, with larger amplitude than those detected at $G = 70$ kg m^{-2} s^{-1} and at almost the same vapor quality. Such waves can be also detected at higher vapor quality ($x = 0.57$) but with smaller amplitude and a much more wrinkled interface with respect to lower x values, due to the increased vapor

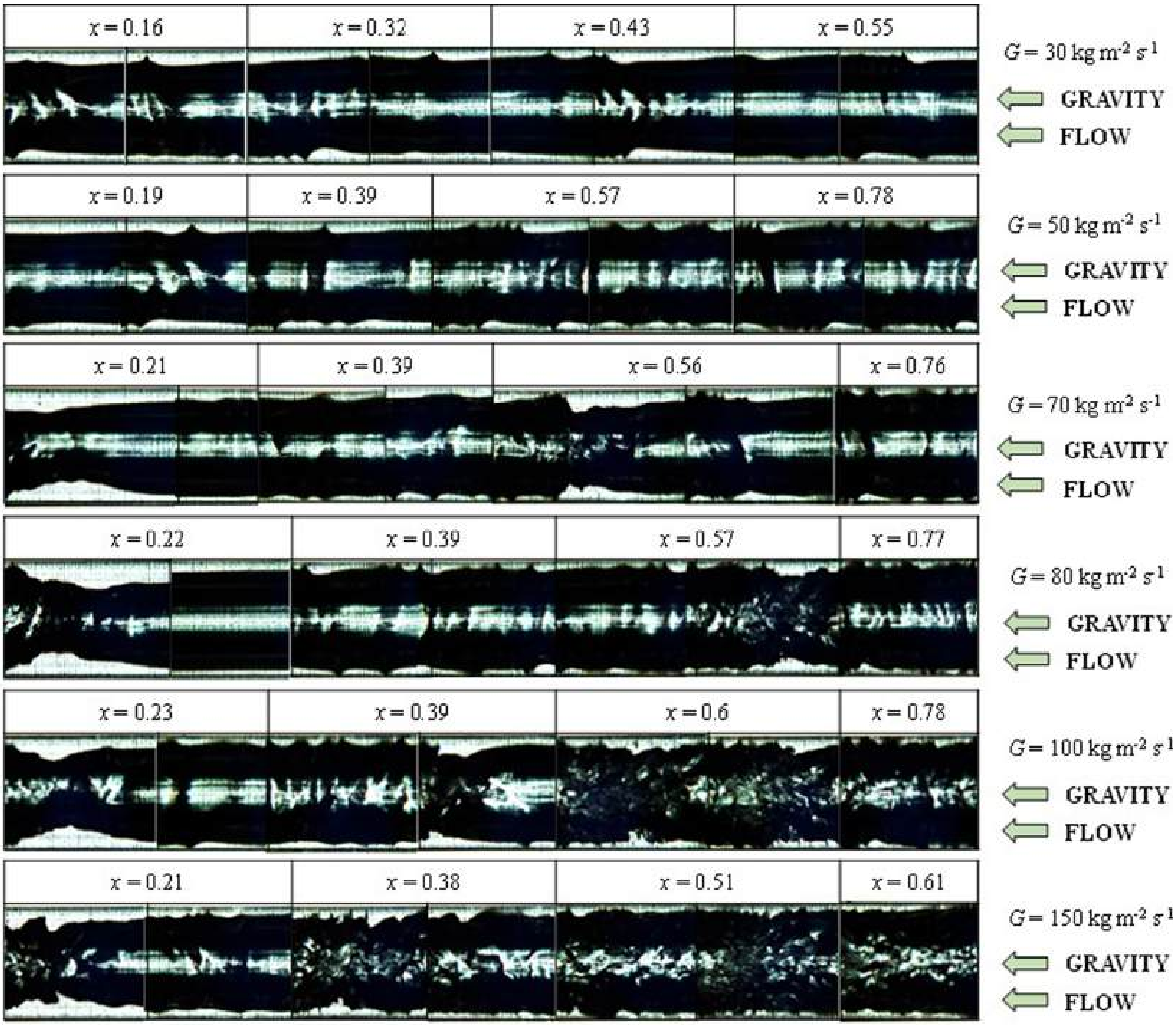

Fig. 8. Flow visualizations of HFE-7000 at mass velocity G equal to 30, 50, 70, 80, 100 and 150 kg m^{-2} s^{-1} and different vapor qualities x during condensation in vertical downflow in the 3.38 mm inner diameter channel.

velocity. Moreover, at $x = 0.56$–0.57 the high-amplitude interfacial waves observed at $G = 80$ kg m^{-2} s^{-1} are more frequent and display a much more irregular shape compared to $G = 70$ kg m^{-2} s^{-1}. Such behaviour can be noticed also at $G = 100$ kg m^{-2} s^{-1}: high-amplitude waves are still detected in a wide range of vapor qualities (from $x = 0.23$ to $x = 0.6$), showing wispy contours with the increasing x values due to the higher vapor shear stress acting on the liquid–vapor interface. In particular, at $x = 0.6$ some liquid parts are found to protrude towards the gas phase and few vapor bubbles are entrained in the liquid flow, while mixing effects in the vapor phase appears to be enhanced compared to smaller vapor quality values. The fluid flow is even more chaotic at $G = 150$ kg m^{-2} s^{-1} where the liquid phase is stretched to be incorporated in the vapor flow at $x = 0.21$ and is then rippled by waves of different frequency and height at $x = 0.38$. At higher vapor quality, a small liquid film is formed at the tube wall with an almost flattened interface and is visibly thinner compared to $G < 150$ kg m^{-2} s^{-1}.

The considerations reported in the present Section are based on a qualitative analysis of the two-phase flow visualizations. A more quantitative approach will be adopted in the following Sections from the analysis of the experimental liquid film thickness data.

4.3. Effect of mass flux and vapor quality on the liquid film thickness of HFE-7000

The experimental data of HFE-7000 can be analysed at various mass fluxes and vapor quality values by calculating the mean and the base liquid film thickness [7,30]. The mean liquid film thickness δ_{mean} is intended as the arithmetic mean of all the instantaneous values δ_i recorded during the acquisition time (3.1 s, for a total of 3110 points):

$$\delta_{mean} = \frac{1}{N}\sum_{i=1}^{N}\delta_i \tag{7}$$

The base liquid film thickness δ_{base}, which is related to the liquid substrate between subsequent high-amplitude waves, is obtained by selecting the M points whose values are smaller than δ_{mean}:

$$\delta_{base} = \frac{1}{M}\sum_{j=1}^{M}\delta_j \qquad \delta_j \leqslant \delta_{mean} \tag{8}$$

The calculated mean and base film thickness values of HFE-7000 are respectively reported in Figs. 9a) and 9b) at mass velocity equal to 50, 70, 80, 100 and 150 kg m^{-2} s^{-1} and at different vapor quality. The mean film thickness is found to decrease with the increasing mass flux at $x \geq 0.4$ due to the enhanced vapor shear stress effect. At low vapor quality ($x < 0.4$), the mean film thickness at $G = 50$ kg m^{-2} s^{-1} is nearly 20%

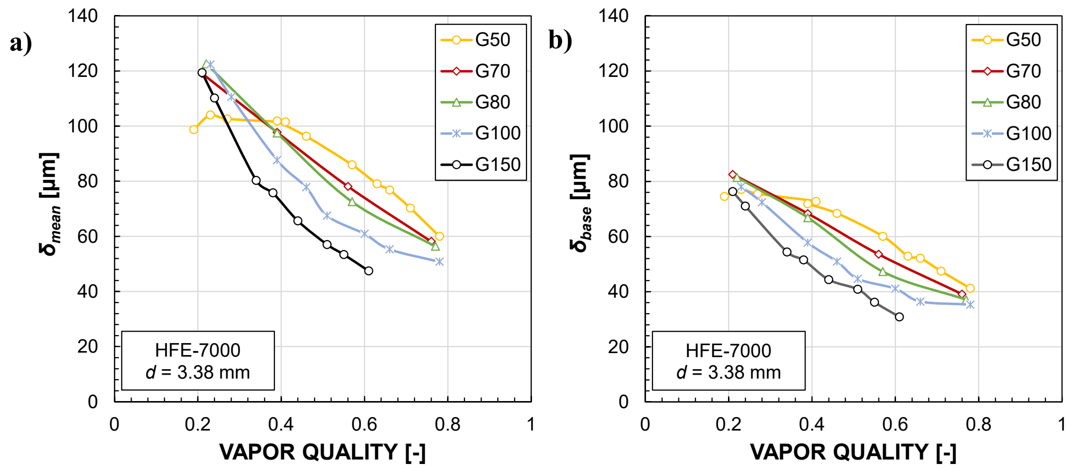

Fig. 9. Experimental mean and base liquid film thickness values of HFE-7000 measured during condensation in vertical downflow inside the 3.38 mm inner diameter channel at mass velocity G from 50 to 150 kg m^{-2} s^{-1}.

smaller with respect to higher mass fluxes. The mean film thickness values at mass flux equal to 70, 80, 100 and 150 kg m^{-2} s^{-1} are almost comparable at low vapor quality ($x \approx 0.2$), while their trends diverge for higher vapor quality.

It is interesting to note that the mean film thickness at $G = 30$ kg m^{-2} s^{-1}, shown in Fig. 3, is about 7–21% smaller compared to $G = 50$ kg m^{-2} s^{-1} in the vapor quality range $x = 0.2$–0.55. Such trend, which was already observed in a previous publication by present authors [30], can be explained considering the transition from shear-driven to gravity-driven condensation in a vertical channel. Indeed, according to Nusselt theory [43], during gravity-driven condensation the liquid film thickness increases with mass flux (at constant vapor quality) due to the higher condensate flow rate. The reduction of the liquid film thickness with the decreasing mass flux was observed also by Beaumale et al. [31], as reported in a recent publication dealing with condensation experiments under vertical downflow at low mass flux (from 5 to 30 kg m^{-2} s^{-1}). Instead, for shear-driven annular flow condensation, the film thickness is reduced with the increasing mass flux (at constant vapor quality) [14].

The base film thickness trend with mass flux and vapor quality is similar to the one observed with δ_{mean} values. At $x \approx 0.2$ the base film thickness at $G = 50$ kg m^{-2} s^{-1} is still slightly smaller (-10%) compared to the one at higher mass flux, which display almost the same value of δ_{base}. At $x \geq 0.3$, the base film thickness reduces with increasing G and x values, with higher deviations between δ_{base} trends observed at intermediate vapor quality ($x = 0.5$–0.6). In particular, the highest deviation (-11%) between δ_{base} values at $G = 80$ kg m^{-2} s^{-1} and $G = 70$ kg m^{-2} s^{-1} is detected at $x = 0.56$–0.57, due to condensate thinning induced by the irregularly shaped and abrupt waves observed at $G = 80$ kg m^{-2} s^{-1} (see Fig. 8).

The mean and base liquid film thickness values of HFE-7000 are reported in Fig. 10 as function of the liquid and vapor superficial velocity j_L and j_G. At constant j_G, both δ_{mean} and δ_{base} values increase with liquid superficial velocity due to the progressively higher liquid loading. Instead, at constant j_L, the film thickness values decrease with the increasing vapor superficial velocity owing to the higher interfacial shear stress. Such behaviour is coherent to what expected for a two-phase annular flow under different liquid/vapor flow rates.

The probability density functions (PDFs) of liquid film thickness of HFE-7000 are reported at four mass fluxes ($G = 50$, 80, 100 and 150 kg m^{-2} s^{-1}) and comparable vapor quality ($x = 0.21$–0.23 and $x = 0.57$–0.61) in Fig. 11. The mean and base film thickness values are also reported in the histograms. At $G = 50$ kg m^{-2} s^{-1} the range of detected film thickness values is quite narrow for both the considered vapor quality, with maximum film thickness of about 300 μm. At $G = 80$ kg m^{-2} s^{-1} a much broader PDF is obtained at $x = 0.22$ compared to $G = 50$ kg m^{-2} s^{-1} due to the occurrence of few disturbance waves displaying 400–600 μm height. However, looking at the PDF the occurrence of high film thickness values is rare and the most probable film thickness is below 100 μm. Instead, at $x = 0.57$ the range of detected film thickness

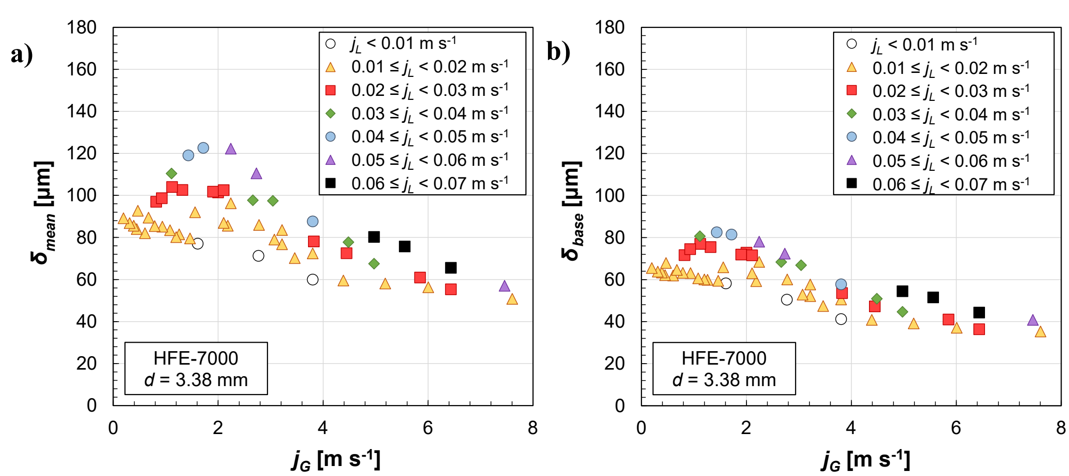

Fig. 10. Experimental mean a) and base b) liquid film thickness values of HFE-7000 measured during condensation in vertical downflow inside the 3.38 mm inner diameter channel, reported as function of the liquid and vapor superficial velocity (j_L and j_G).

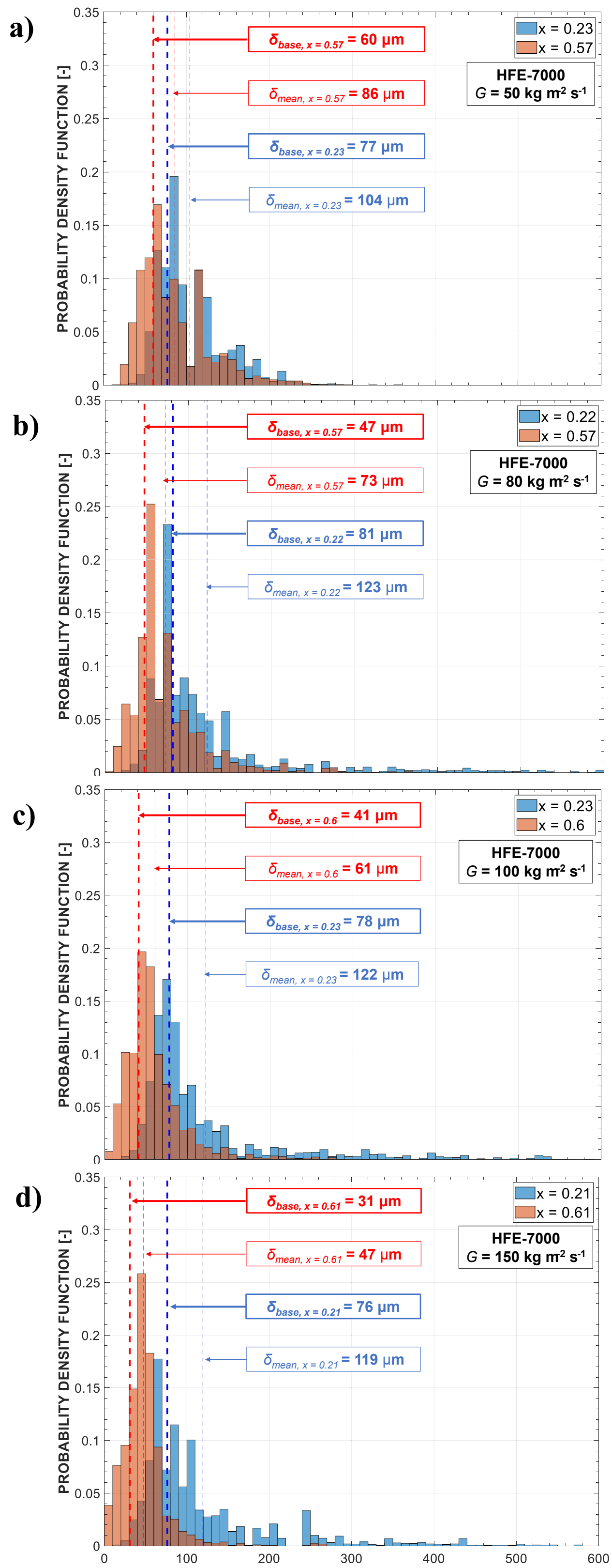

Fig. 11. Probability density function (PDF) of liquid film thickness values of HFE-7000 measured at different mass flux and comparable vapor quality (x = 0.21–0.23 and x = 0.57–0.61): a) G = 50 kg m^{-2} s^{-1}, b) G = 80 kg m^{-2} s^{-1}, c) G = 100 kg m^{-2} s^{-1}, d) G = 150 kg m^{-2} s^{-1}.

values is similar to that at $G = 50$ kg m^{-2} s^{-1}, with a shift of the PDF peak towards a smaller value. High-amplitude interfacial instabilities are still present even at $G = 100$ kg m^{-2} s^{-1} and $G = 150$ kg m^{-2} s^{-1} at low vapor quality, hence contributing to the thinning of the mean and base liquid film. Instead, at x = 0.6–0.61 and G = 100–150 kg m^{-2} s^{-1} the PDF curve does not exceed 300 μm and the most probable film thickness values are almost all concentrated below 100 μm.

It is clear from Fig. 11 that the mean film thickness is not representative of the most probable film thickness in the PDF. Instead, the base film thickness is much closer to the PDF peak for the considered operating conditions and such result is in agreement with the recent findings by Wang et al. [16]. From previous studies during condensation in vertical downflow [29], it emerges that the base film thickness is more linked to heat transfer, especially at low and intermediate vapor quality, since the main thermal resistance is concentrated in the liquid substrate after the passage of high-amplitude waves.

To complete the characterization of the interfacial features, the power spectral density (PSD) in the frequency domain of the liquid film thickness records of HFE-7000 is calculated. The PSDs are obtained averaging the results of the Welch algorithm, using a Hamming window of length equal to 1024 samples and with 50% overlap. The considered liquid film thickness time traces account for about 3110 points, corresponding to 1000 Hz acquisition frequency over a time interval of 3.1 s. Large PSD values are obtained in correspondence of disturbance waves, i.e. high-amplitude waves. Fig. 12 shows the PSDs of wave frequency of HFE-7000 at mass flux equal to 50, 80, 100 and 150 kg m^{-2} s^{-1} and at two different vapor quality (x = 0.21–0.23 and x = 0.57–0.61). At G = 50 kg m^{-2} s^{-1} the PSDs are comparable at x = 0.23 and x = 0.57, with a frequency peak at about 22 Hz and 24 Hz, respectively. At G = 80 kg m^{-2} s^{-1} and x = 0.22 the PSD curve displays a peak at 16 Hz, thus at a lower frequency with respect to G = 50 kg m^{-2} s^{-1}, while the range of detected frequencies becomes larger. Indeed, at this operating condition there is the coexistence of high-amplitude waves, having frequencies of about 15–20 Hz, and smaller ripples with higher frequency (around 50 Hz). At x = 0.57, the PSD curve is much more flattened with respect to x = 0.23 due to the reduction of the liquid film thickness with increasing vapor quality. The PSD shape at G = 100 kg m^{-2} s^{-1} and x = 0.23 is similar to the one observed at G = 80 kg m^{-2} s^{-1} and at the same vapor quality. The PSD covers frequencies up to 200 Hz and displays a peak around 18 Hz. The same can be argued for G = 150 kg m^{-2} s^{-1} at x = 0.21, although the frequency peak is shifted towards higher values (f_w = 31 Hz) and the amplitude of the PSD is reduced due to the smaller height of the disturbance waves. At x = 0.6–0.61, the PSD curves at both G = 100–150 kg m^{-2} s^{-1} are flattened, highlighting the occurrence of small-amplitude interfacial ripples with various frequency (mainly within 0–100 Hz).

When high-amplitude disturbance waves are present (G = 80 kg m^{-2} s^{-1} and G = 100 kg m^{-2} s^{-1}), the entrainment of vapor bubbles in the condensate film can be observed [44,45]. Indeed, Figs. 13 and 14 show the entrapment of vapor in the liquid film in the form of bubbles of various sizes at both G = 80 kg m^{-2} s^{-1} and G = 100 kg m^{-2} s^{-1}. The presence of vapor bubbles in the liquid film is reported in many experimental papers in which visualisations of gas-sheared liquid film were performed by means of various optical methods [18,46,47]. The gas bubbles inside the liquid film are expected to play an important role in the flow dynamics. The presence of bubbles may change the overall effective flow dynamic parameters of liquid film, such as density and viscosity. Moreover, vapor bubbles can contribute to an increase in the interfacial area. Between an entrapped vapor bubble and the tube wall an area of locally much thinner film exists and, consequently, a much higher heat transfer rate is obtained [48]. As concluded by Zadrazil et al. [3], which experimentally measured the frequency and the size distribution of the entrained vapor bubbles during annular flow, the vapor entrainment is strictly related to the appearance of large-amplitude waves.

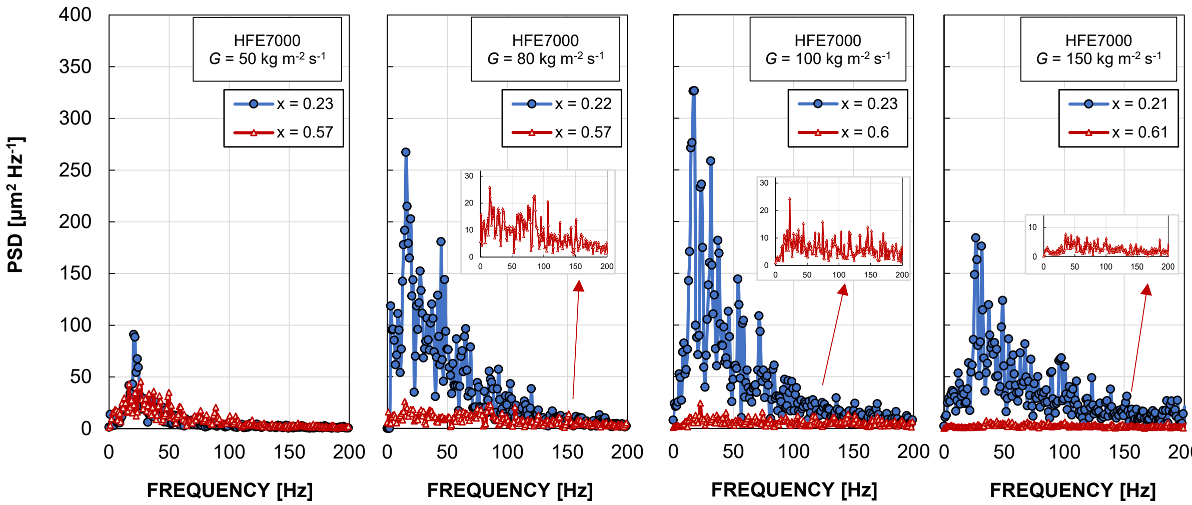

Fig. 12. Power spectral density (PSD) of wave frequency for HFE-7000 obtained using the Welch method, at mass flux equal to 50, 80, 100 and 150 kg m^{-2} s^{-1} and vapor quality values x = 0.21–0.23 and x = 0.57–0.61.

4.4. Comparison in terms of film thickness values among fluids

The experimental liquid film thickness data of HFE-7000 are here compared against those of R245fa and R134a, which were tested during previous condensation campaigns using the same setup located in Padova (Italy) [29,30]. As indicated in Table 2, R134a was tested at 30 °C saturation temperature (corresponding to p_{sat} = 7.7 bar) to avoid exceeding the maximum allowable pressure for the borosilicate glass tube, equal to 9 bar, and prevent any breakage. The thermodynamic and transport properties of R245fa, R134a and HFE-7000, reported in Table 2, are computed at the test conditions using REFPROP 10.0 [36]. Fluid HFE-7000 displays the lowest vapor density and the highest liquid viscosity compared to the R245fa and R134a.

The mean and base film thickness data of R245fa and R134a are already reported in the works of Berto et al. [29,30]. In order to highlight the differences in terms of interfacial characteristics among R245fa, R134a and HFE-7000, the corresponding film thickness standard deviation is reported in Fig. 15 at mass flux equal to 50, 75–80 and 100 kg m^{-2} s^{-1}, at different vapor quality values. As shown in Fig. 15, at G = 50 kg m^{-2} s^{-1} the standard deviations for R245fa and HFE-7000 are comparable, therefore the height of the interfacial instabilities is almost similar between the two fluids. With regard to R134a, the standard deviation of liquid film thickness is about 16–33% smaller compared to R245fa and HFE-7000 in the whole vapor quality range. This can be due to the higher vapor density of R134a which causes lower vapor velocity at the same mass flux and vapor quality, hence leading to more restrained interfacial waviness. Such behaviour is observed also at G = 75–80 kg m^{-2} s^{-1}: the standard deviations for R134a are much smaller than those of R245fa and HFE-7000 especially at x = 0.2–0.5, while reaching the same value at x > 0.75. The film thickness standard deviations of R245fa varies from 118 µm at x = 0.19 down to about 30 µm at x = 0.79 and are slightly higher than those obtained with HFE-7000, although displaying the same general trend with vapor quality. The high standard deviations obtained at small vapor quality with these fluids can be explained considering the appearance of disturbance waves induced by the vapor shear stress acting on the liquid–vapor interface, as documented by flow visualizations and statistical analyses [29]. At G = 100 kg m^{-2} s^{-1} the film thickness standard deviation trends of R245fa and HFE-7000 are still comparable, especially at x > 0.4. Instead, the film thickness standard deviations of R134a are higher than those of R245fa and HFE-7000 in the whole range of considered vapor quality values (x = 0.48–0.84). Indeed, as reported in [30], at such mass flux high-amplitude interfacial instabilities are also detected with R134a. As pointed out in previous studies [29,30], the appearance of high-amplitude and fast disturbance waves in the case of both R245fa and R134a is responsible for a heat transfer enhancement as compared to smaller mass fluxes.

In order to better understand the results shown in Fig. 15, the time traces of liquid film thickness for the three considered fluids are reported at almost the same vapor quality (x = 0.55–0.6) and at mass flux equal to 50, 75–80 and 100 kg m^{-2} s^{-1} in Figs. 16-18. The mean and base film thickness values are also depicted in the figures. As already observed in Fig. 15, at G = 50 kg m^{-2} s^{-1} the interfacial waviness is weak for R134a, while disturbance waves with maximum height of 580 µm and 300–350 µm are respectively detected in the case of R245fa and HFE-7000 even at this low mass flux. At such conditions, the smallest mean and base film thickness values are obtained with R134a. This finding can be explained considering the reduced contribution of the vapor velocity at such mass flux and the small liquid viscosity of R134a (μ_L = 183.13 µPa s, see Table 2), which promotes the thinning of the liquid film in agreement with Nusselt [43] theory. Slightly higher δ_{mean} and δ_{base} values are observed with HFE-7000, which may result from the competition between the high vapor velocity (ρ_G = 10.26 kg m^{-3}) and the high liquid viscosity, which nearly doubles that of R134a at saturation temperature. Instead, the mean and base film thickness of R245fa are respectively 18% and 20% higher than those of HFE-7000. Although HFE-7000 displays a slightly higher liquid viscosity (+7%), its small vapor density (being 27% lower as compared to R245fa) is expected to play the major role in the thinning of the liquid film.

At G = 75–80 kg m^{-2} s^{-1}, the lowest mean and base film thickness values are detected with HFE-7000. However, at comparable working conditions, the interfacial waviness is much more pronounced for R245fa despite the smaller vapor velocity and the similar liquid viscosity compared to HFE-7000. Such result can be explained comparing the temporal film thickness evolution of R245fa at G = 80 kg m^{-2} s^{-1} with that of HFE-7000 at smaller mass flux (G = 60 kg m^{-2} s^{-1}) and at the same vapor quality, which is reported in Fig. 19. At such condition, the temporal film thickness profile of HFE-7000 is characterized by high-amplitude waves, which are almost comparable to those of R245fa in terms of height although being less frequent. Moreover, the mean and base film thickness values are similar between R245fa and HFE-7000 at the two different operating conditions. Such comparison suggests that the inception of high-amplitude waves, which promotes the thinning of the liquid film, can be observed at smaller mass flux for HFE-7000 due to the lower vapor density and, hence, increased vapor shear stress (at fixed G and x values). Therefore, since the liquid viscosities of R245fa

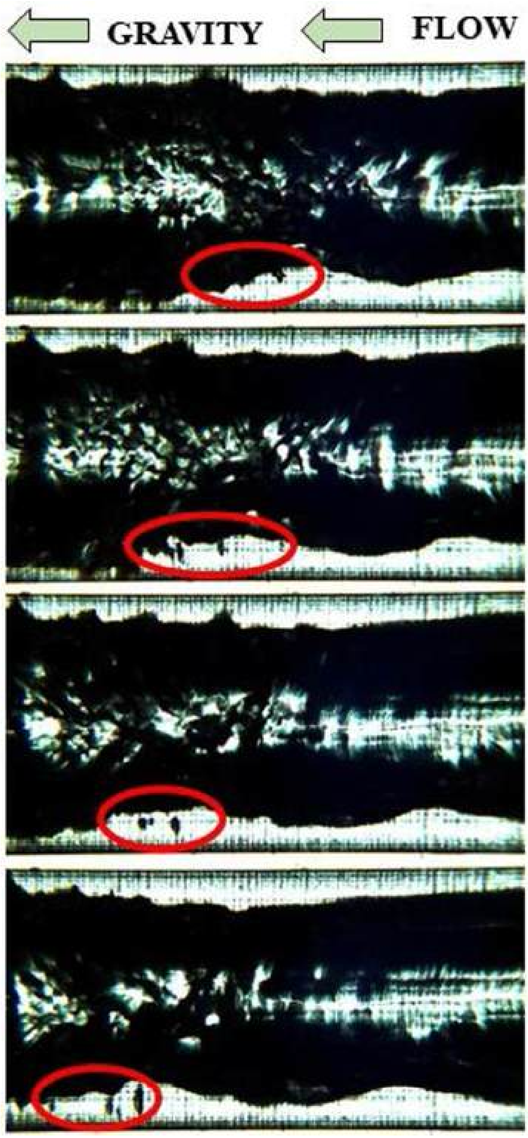

Fig. 13. Entrainment of vapor bubbles in the liquid film of HFE-7000 at mass flux $G = 80$ kg m^{-2} s^{-1} and vapor quality $x = 0.39$ during condensation in vertical downflow inside the 3.38 mm inner diameter channel.

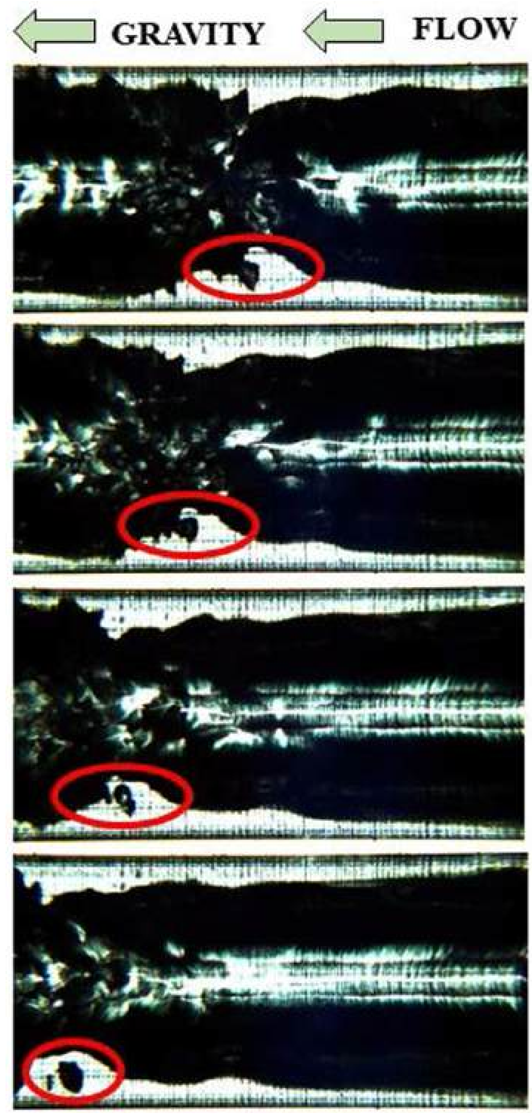

Fig. 14. Entrainment of vapor bubbles in the liquid film of HFE-7000 at mass flux $G = 100$ kg m^{-2} s^{-1} and vapor quality $x = 0.4$ during condensation in vertical downflow inside the 3.38 mm inner diameter channel.

and HFE-7000 are very similar but the vapor density is higher for R245fa ($\rho_{G,R245fa}/\rho_{G,HFE\text{-}7000} = 1.4$), similar interfacial waves characteristics can be found when comparing R245fa results at $G = 80$ kg m^{-2} s^{-1} with HFE-7000 results at $G = 60$ kg m^{-2} s^{-1} (with a ratio of vapor superficial velocities nearly equal to one). At $G = 75$–80 kg m^{-2} s^{-1} the highest mean and base film thickness values are detected with R134a, whose liquid–vapor interface is indeed affected by a limited waviness due to the high density of the vapor phase. It can be noted that for R134a δ_{mean} and δ_{base} values at $G = 75$ kg m^{-2} s^{-1} are respectively 34% and 16% higher than those at $G = 50$ kg m^{-2} s^{-1}. This can be explained considering gravity-controlled condensation. Instead, for R245fa and HFE-7000, the condensation is clearly affected by vapor shear stress also at such low values of mass velocity with a reduction of the liquid film thickness when moving from 50 to 80 kg m^{-2} s^{-1}.

The onset of disturbance waves can be detected at higher mass fluxes for R134a, as shown in Fig. 17. Indeed, at $G = 100$ kg m^{-2} s^{-1} various interfacial disturbances with maximum height equal to 700–800 μm appear, leading to 20% smaller base film thickness with respect to $G = 75$ kg m^{-2} s^{-1}. However, such disturbance waves are not sufficient for reaching the small film thickness values of R245fa and HFE-7000, which are indeed favoured by the greater vapor shear stress (at the same mass flux and vapor quality). The lowest δ_{mean} and δ_{base} values are obtained with HFE-7000, which are 33–35% and 7–8% smaller compared to R134a and R245fa, respectively.

With the aim to clearly identify the range of wave frequencies for the three considered fluids, the power spectral density (PSD) in the frequency domain of the liquid film thickness data is calculated using the

Table 2
Thermodynamic and transport properties of R245fa, R134a and HFE-7000 at the studied test conditions [36].

Fluid	R245fa	R134a	HFE-7000
p_{sat} [bar]	2.51	7.70	1.25
p_{red} [-]	0.07	0.19	0.05
T_{sat} [°C]	40	30	40
ρ_L [kg m^{-3}]	1296.7	1187.5	1362.5
ρ_G [kg m^{-3}]	14.12	37.54	10.26
μ_L [μPa s]	328.6	183.13	350.98
λ_L [mW m^{-1} K^{-1}]	83.36	78.99	62.16
h_{LG} [kJ kg^{-1}]	182.31	173.10	131.17
σ [mN m^{-1}]	11.73	7.38	10.7

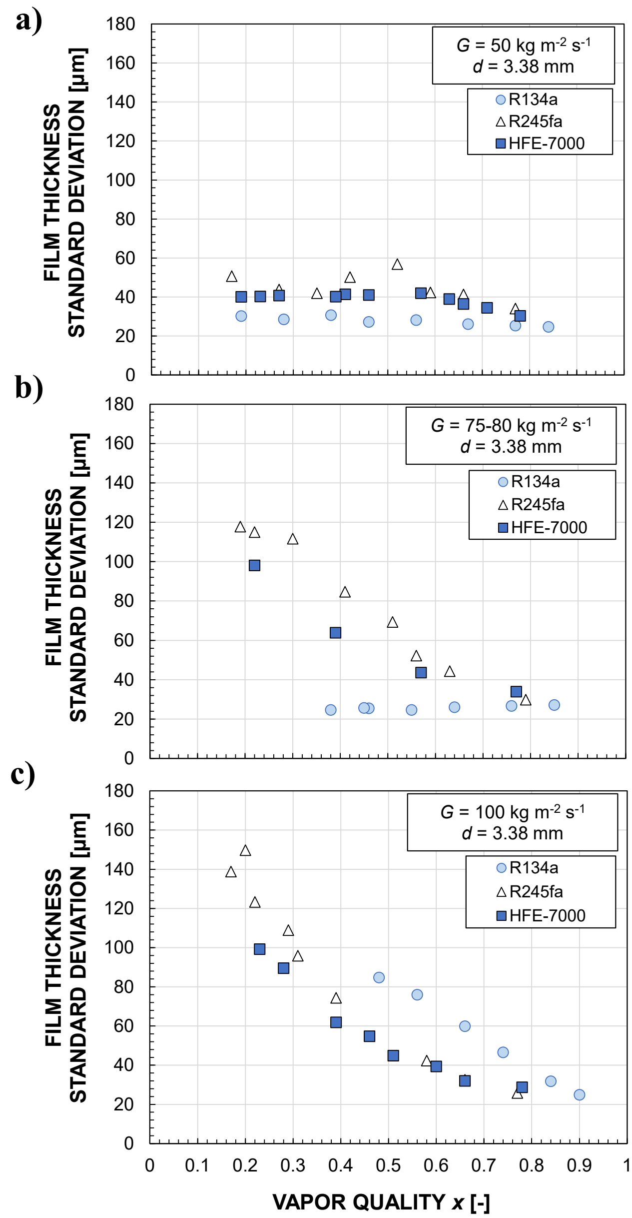

Fig. 15. Standard deviation of the instantaneous film thickness values for R245fa, R134a and HFE-7000 vs. vapor quality (and mass flux) during vertical downflow condensation inside the 3.38 mm inner diameter channel: a) $G = 50$ kg m^{-2} s^{-1}, b) $G = 75$–80 kg m^{-2} s^{-1}, c) $G = 100$ kg m^{-2} s^{-1}.

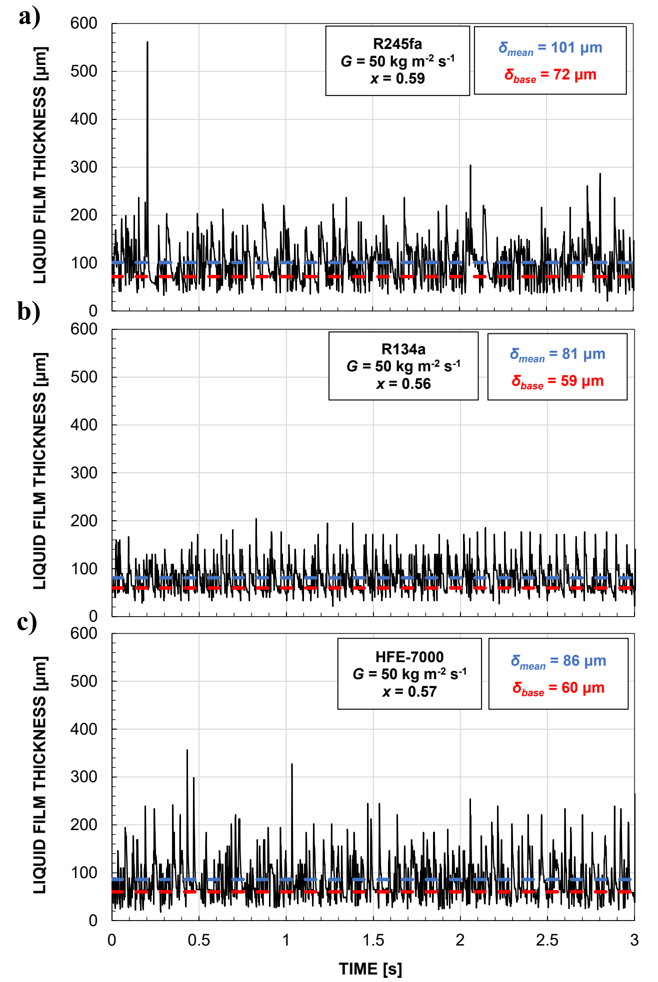

Fig. 16. Temporal evolution of the liquid film thickness at $G = 50$ kg m^{-2} s^{-1} and comparable vapor quality during condensation in vertical downflow: a) R245fa at $x = 0.59$, b) R134a at $x = 0.56$, c) HFE-7000 at $x = 0.57$. The mean and base film thickness values are also indicated.

Welch algorithm. Fig. 20 depicts the PSDs of wave frequency of R245fa, R134a and HFE-7000 at $G = 50$ kg m^{-2} s^{-1} and at $x = 0.56$–0.59. The PSDs of R245fa and HFE-7000 display a similar shape, with the frequency peak at 14 Hz and at 25 Hz respectively. At such condition, both sporadic high-amplitude waves (displaying low frequency) and ripples, having smaller height and larger frequency (of about 60 Hz for R245fa and 90 Hz for HFE-7000) can be detected for both R245fa and HFE-7000. The PSD of these two fluids cover frequencies up to about 100 Hz. With regard to R134a, the detected wave frequencies are mainly in the range 0–50 Hz.

With the increasing mass flux ($G = 75$–80 kg m^{-2} s^{-1}), as shown in Fig. 21, the PSD of R245fa is still sharp with slightly higher PSD peak amplitude compared to $G = 50$ kg m^{-2} s^{-1} due to the appearance of disturbance waves. With regard to HFE-7000, the most important frequencies are concentrated in the 20–120 Hz range, whereas for R134a the PSD is flattened.

Fig. 22 shows the PSDs of wave frequency of R245fa, R134a and HFE-7000 at $G = 100$ kg m^{-2} s^{-1} and at $x = 0.56$–0.6. At $G = 100$ kg m^{-2} s^{-1} the PSD of R134a shows a peak at 16 Hz, corresponding to the dominant frequency of the disturbance waves which are first observed at this mass flux. Instead, the smaller amplitude waves display frequencies in the 30–70 Hz range.

From this analysis it can be concluded that HFE-7000 displays smaller film thickness values compared to R245fa and R134a at $G \geq 80$ kg m^{-2} s^{-1}. At lower mass fluxes, the small liquid viscosity of R134a is responsible for the thinning of the liquid film with respect to the other fluids. Moreover, HFE-7000 seems to lead to the earlier inception of high-amplitude waves due to its smaller vapor density compared to the other fluids.

5. Assessment of models for the prediction of the mean film thickness

Due to the limited quantitative data of local and instantaneous film thickness, the main characteristics of micro-scale condensing flows are not fully understood, and thus the accurate design of microchannel condensers still remains a difficult task. It is reported that the thickness of the liquid film is one of the most important parameters for predicting two phase heat transfer in micro tubes, especially inside vertical channels [14,49–51]. Lots of analytical expressions and empirical correlations for predicting the mean liquid film thickness and the disturbance

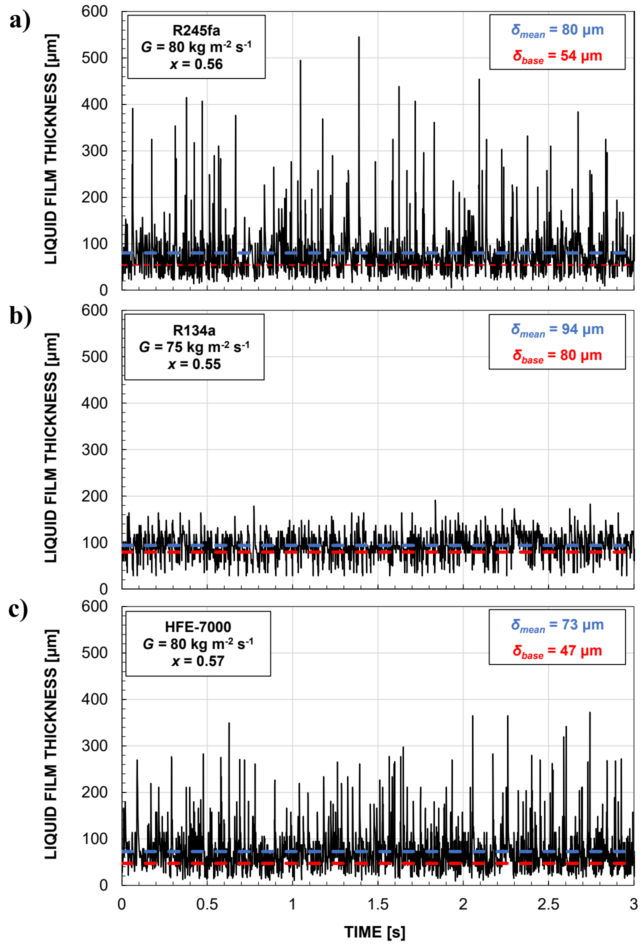

Fig. 17. Temporal evolution of the liquid film thickness at $G = 75$–80 kg m^{-2} s^{-1} and comparable vapor quality during condensation in vertical downflow: a) R245fa at $x = 0.56$, b) R134a at $x = 0.55$, c) HFE-7000 at $x = 0.57$. The mean and base film thickness values are also indicated.

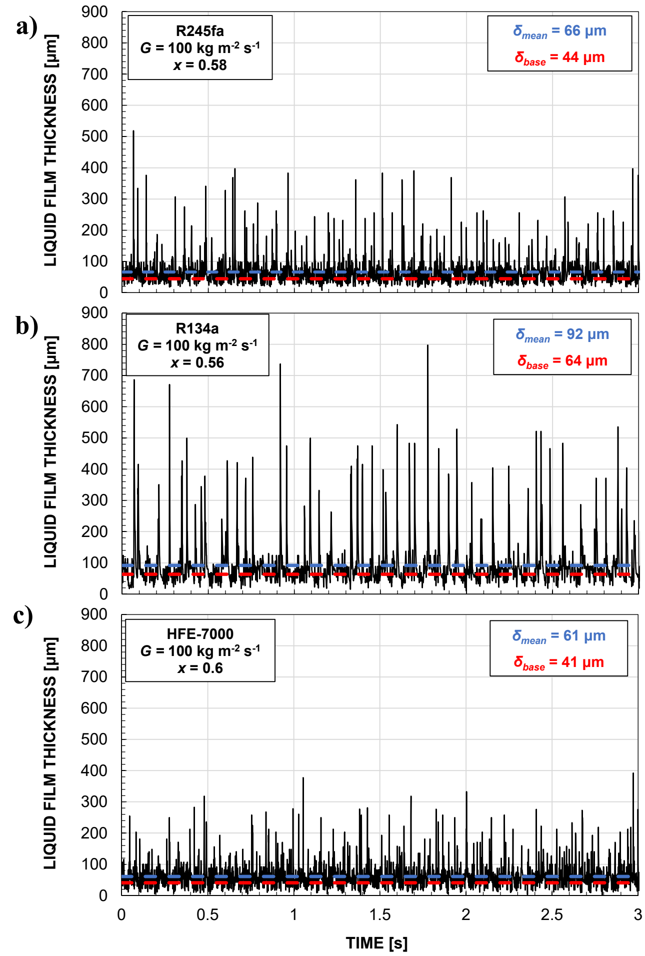

Fig. 18. Temporal evolution of the liquid film thickness at $G = 100$ kg m^{-2} s^{-1} and comparable vapor quality during condensation in vertical downflow: a) R245fa at $x = 0.58$, b) R134a at $x = 0.56$, c) HFE-7000 at $x = 0.6$. The mean and base film thickness values are also indicated.

wave characteristics have been proposed [12,22,52–57].

In order to check the reliability of the existing predicting methods, the experimental mean film thickness data of HFE-7000 are here compared against the predictions from the models by Nusselt [43], Cavallini et al. [58] with Del Col et al. [59] correlation for the wall shear stress τ_{wall} and Cioncolini et al. [60] with Wallis [61] correlation.

The correlation by Nusselt et al. [43] for predicting the mean liquid film thickness is given by Eq. (9):

$$\delta = 0.9\cdot\left[\frac{\mu_L\cdot G\cdot(1-x)\cdot d}{\rho_L\cdot(\rho_L-\rho_G)\cdot g}\right]^{1/3} = 0.9\cdot\left[\frac{\mu_L^2}{\rho_L\cdot(\rho_L-\rho_G)\cdot g}\right]^{1/3}\cdot Re_F^{1/3} \quad (9)$$

where ρ_G and ρ_L are the vapor and liquid density, μ_L is the liquid dynamic viscosity, g is the gravity acceleration and Re_F is the Reynolds number of the liquid film, calculated with Eq. (10):

$$Re_F = \frac{G\cdot(1-x)\cdot(1-\varepsilon)\cdot d}{\mu_L} \quad (10)$$

In Eq. (10) ε is the entrained liquid fraction. At the tested mass fluxes the entrained liquid fraction is always below 0.08 according to Cioncolini et al. [60].

The dimensionless liquid film thickness δ^+ by Cavallini et al. [58] and Cioncolini et al. [60] are respectively calculated using Eqs. (11)–(12):

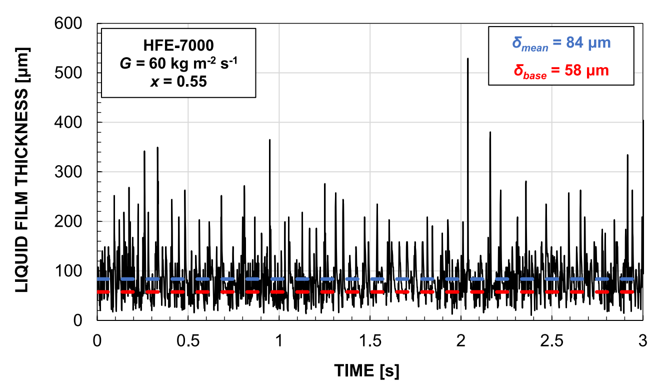

Fig. 19. Temporal evolution of the liquid film thickness of HFE-7000 at $G = 60$ kg m^{-2} s^{-1} and $x = 0.55$. The mean and base film thickness values are also indicated.

$$\delta^+ = \begin{cases} (Re_F/2)^{0.5} & \text{for } Re_F \leqslant 1145 \\ 0.0504\cdot Re_F^{7/8} & \text{for } Re_F > 1145 \end{cases} \quad (11)$$

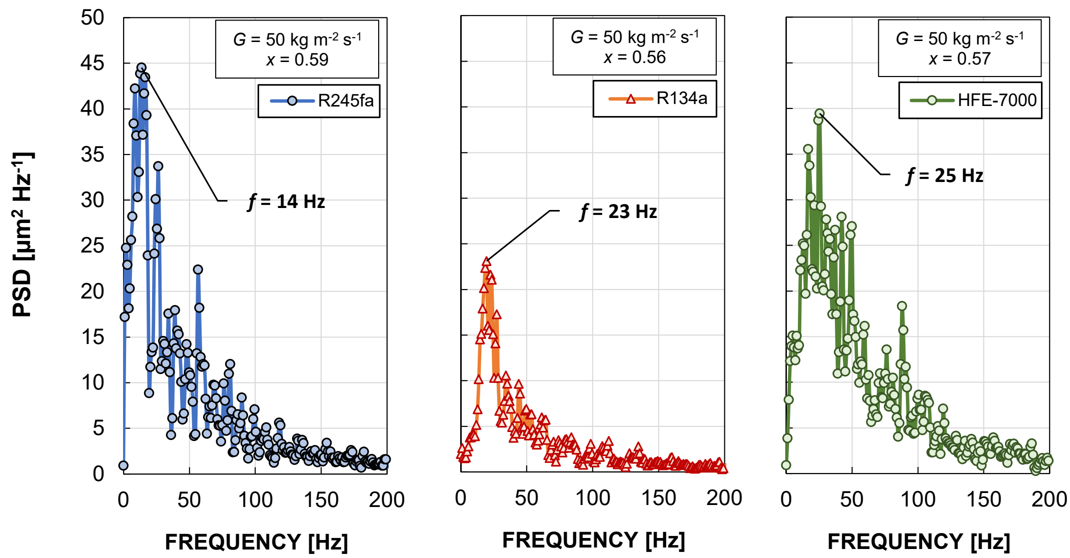

Fig. 20. Power spectral density (PSD) of wave frequency at mass flux equal to 50 kg m^{-2} s^{-1} and vapor quality x = 0.56–0.59 for R245fa (left), R134a (center) and HFE-7000 (right).

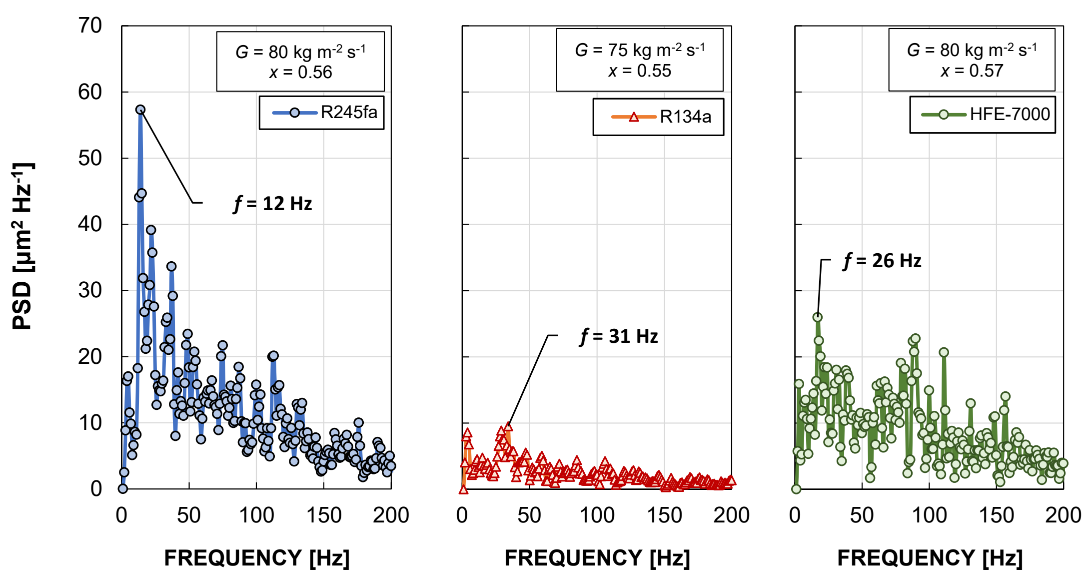

Fig. 21. Power spectral density (PSD) of wave frequency at mass flux equal to 75–80 kg m^{-2} s^{-1} and vapor quality x = 0.55–0.57 for R245fa (left), R134a (center) and HFE-7000 (right).

$$\delta^{+} = \begin{cases} (\mathrm{Re}_F/2)^{0.5} \text{ for } \mathrm{Re}_F \leqslant 162 \\ 0.6246 \cdot \mathrm{Re}_F^{0.5244} \text{ for } 162 < \mathrm{Re}_F < 2785 \\ 0.03221 \cdot \mathrm{Re}_F^{0.8982} \text{ for } \mathrm{Re}_F \geqslant 2785 \end{cases} \quad (12)$$

Such values are then used to calculated the mean liquid film thickness according to Eq. (13):

$$\delta = \delta^{+} \cdot \frac{\mu_L}{(\rho_L \cdot \tau_{wall})^{0.5}} \quad (13)$$

where ρ_L is the liquid density and τ_{wall} is the wall shear stress, defined as in Eq. (14):

$$\tau_{wall} = f_{wall} \cdot \frac{\rho_L \cdot j_L^2}{2 \cdot (1-\varepsilon)^2} = \left(\frac{\mathrm{d}p}{\mathrm{d}z}\right) \cdot \frac{d}{4} \quad (14)$$

In Eq. (14) f_{wall} is the friction factor at the tube wall, j_L is the superficial velocity of the liquid phase and (dp/dz) is the frictional pressure gradient along the channel. According to Wallis [61] correlation, f_{wall} is calculated with Eq. (15):

$$f_{wall} = 16 \cdot \mathrm{Re}_L^{-1} \quad (15)$$

and the entrained liquid fraction is obtained by the following equations:

$$\frac{\varepsilon^{5/2}}{(1-\varepsilon)^2 \cdot [1 + 150 \cdot (1 - \varepsilon^{0.5})]} = R^{-1} \quad (16)$$

$$R = \frac{16 \cdot Re_L}{0.046 \cdot Re_G^{-1.2}} \cdot \frac{\rho_G}{\rho_L} \cdot \left(\frac{1-x}{x}\right)^2 \quad (17)$$

In Eqs. (15)–(17) Re_L and Re_G are respectively the liquid and vapor Reynolds numbers.

The wall shear stress can be also calculated following the Cavallini

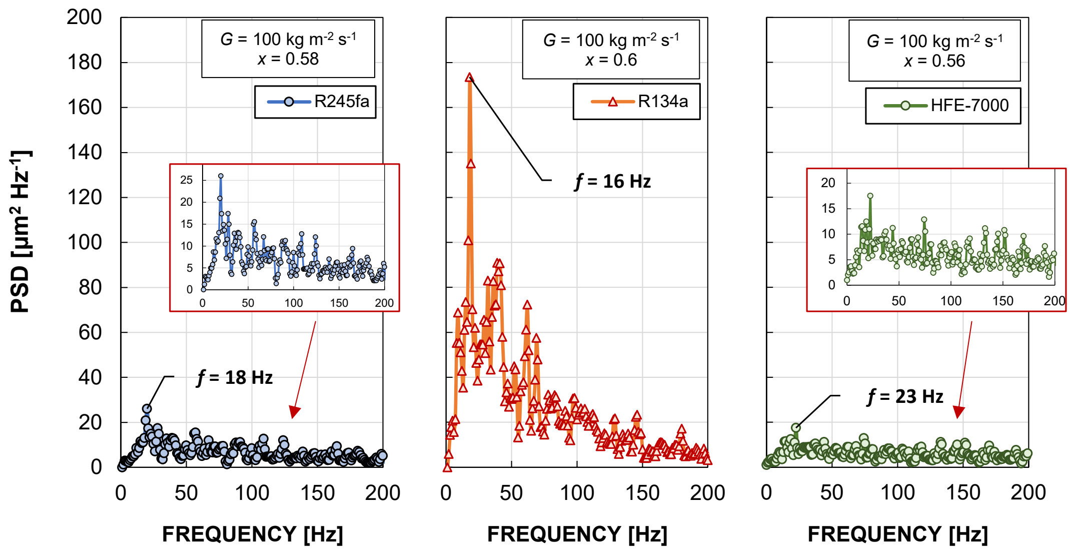

Fig. 22. Power spectral density (PSD) of wave frequency at mass flux equal to 100 kg m^{-2} s^{-1} and vapor quality x = 0.56–0.60 for R245fa (left), R134a (center) and HFE-7000 (right).

et al. [58] approach, based on the calculation of the two-phase frictional multiplier Φ_{LO}:

$$\left(\frac{\mathrm{d}p}{\mathrm{d}z}\right) = \Phi_{LO}^2 \cdot \frac{2 \cdot f_{LO} \cdot G^2}{\rho_L \cdot d} \tag{18}$$

where f_{LO} is the friction factor of the liquid phase flowing alone in the tube and Φ_{LO} is evaluated as reported in Cavallini et al. [58]. In the present work, f_{LO} is calculated according to Del Col et al. [59] correlation:

$$f_{LO} = 0.046 \cdot Re_{LO}^{-0.2} + 0.7 \cdot RR \cdot X \tag{19}$$

where Re_{LO} is the Reynolds number of the liquid phase flowing alone in the channel, RR and X are evaluated using Eqs. (20)–(21):

$$RR = \frac{2 \cdot Ra}{d} \tag{20}$$

$$X = \begin{cases} 0 \text{ for } \mathrm{Re}_{LO} \leqslant Re_{LO}^{+} \\ 1 \text{ for } \mathrm{Re}_{LO} \geqslant 3500 \\ 1 + \dfrac{8.9938 \cdot 10^{-3} - 0.046 \cdot Re_{LO}^{-0.2}}{0.7 \cdot RR} \text{ for } Re_{LO}^{+} < \mathrm{Re}_{LO} < 3500 \end{cases} \tag{21}$$

In Eq. (20), Ra is the internal surface roughness of the channel (equal to 0.18 μm in the present case), while in Eq. (21) Re_{LO}^{+} is defined as follows:

$$Re_{LO}^{+} = \left(\frac{8.9938 \cdot 10^{-3} + 0.7 \cdot RR}{0.046}\right) \tag{22}$$

Fig. 23 shows the comparison between experimental and predicted mean liquid film thicknesses of HFE-7000. Table 3 reports the mean relative deviation e_R, mean absolute deviation e_{AB} and standard deviation σ_N between experimental and calculated δ_{mean} values of HFE-7000. The model by Nusselt [43] provides accurate predictions of the mean liquid film thickness of HFE-7000 at $G \leq 30$ kg m^{-2} s^{-1}, as the mean absolute deviation between experimental and calculated values is smaller than 8.2% and 19.7% at $G = 20$ kg m^{-2} s^{-1} ($\sigma_N = 0.51\%$) and $G = 30$ kg m^{-2} s^{-1} ($\sigma_N = 2.25\%$), respectively. Such good agreement between experimental δ_{mean} values and calculated ones confirms the limited shear stress effect at the liquid–vapor interface at these small mass fluxes and the more significant contribution of gravity acceleration. With the increasing mass flux, the experimental film thickness values are largely overestimated by Nusselt [43] model, especially at high vapor quality, due to the enhanced vapor shear stress effect on the liquid–vapor interface.

The model of Cavallini et al. [58] with Del Col et al. [59] correlation for wall shear stress τ_{wall} leads to more accurate predictions at $G > 60$ kg m^{-2} s^{-1} ($e_{AB} = 10.92\%$ and $\sigma_N = 10.52\%$). However, the prediction accuracy at lower mass velocities is much smaller as compared to Nusselt [43] model ($e_{AB} = 78.25\%$). The same can be argued for Cioncolini et al. [60] model with Wallis [61] correlation for τ_{wall}. The predictive accuracy is satisfactory at $G = 150$ kg m^{-2} s^{-1} (relative errors lower than 11% for all points), while much higher deviations are observed at smaller mass fluxes. At $G = 20$–30 kg m^{-2} s^{-1} the experimental data are severely overpredicted ($e_{AB} = 58.45\%$). Instead, in the mass flux range from 40 to 70 kg m^{-2} s^{-1} δ_{mean} values at high vapor quality are generally underpredicted, while the opposite occurs at small vapor quality. A similar behaviour has been partly observed also for the predictions from Cavallini et al. [58] model. Therefore, it can be speculated that these two models do not accurately predict the effect of interfacial waves on the film thickness for mass fluxes lower than 100 kg m^{-2} s^{-1}.

6. Conclusions

In the present study, liquid film thickness measurements are performed during vertical downflow condensation inside a 3.38 mm inner diameter channel at 40 °C saturation temperature. Condensation tests are carried out with HFE-7000 in two separate experimental apparatuses: the first is composed of two counter-flow tube-in-tube heat exchangers separated by an adiabatic borosilicate glass tube for flow visualizations and film thickness measurement, whereas the second consists of a diabatic sapphire tube coupled with an infrared camera for simultaneous local heat flux and film thickness measurements at low mass flux (5–30 kg m^{-2} s^{-1}). Various optical techniques (chromatic confocal imaging, interferometry, shadowgraphy) are employed in the two independent labs for measuring the liquid film thickness.

The main conclusions are here summarized:

- Comparable film thickness values, wave heights and wave frequencies are obtained in the two experimental test sections at the same working conditions ($G = 20$–30 kg m^{-2} s^{-1}). Such result is even more significant considering the differences between the two experimental setups (adiabatic glass tube in one case, diabatic sapphire test section in the other) and the different optical methods

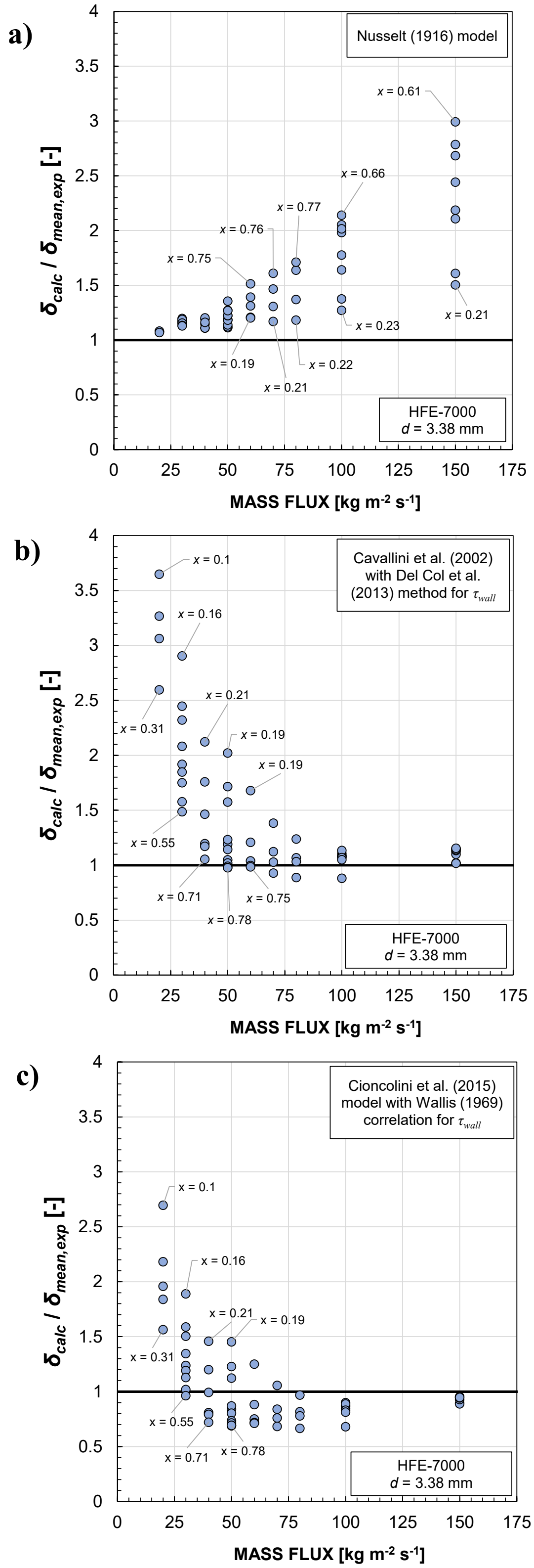

Fig. 23. Comparison between experimental mean liquid film thicknesses of HFE-7000 during condensation at 40 °C saturation temperature in the 3.38 mm inner diameter channel and predicted values from the models by a) Nusselt [43], b) Cavallini et al. [58] with Del Col et al. [59] correlation and c) Cioncolini et al. [60] with Wallis [61] correlation for the calculation of τ_{wall}. G is the mass velocity [kg m^{-2} s^{-1}].

Table 3
Mean relative deviation e_R, mean absolute deviation e_{AB} and standard deviation σ_N between the experimental mean liquid film thicknesses and predicted values during condensation of HFE-7000.

HFE-7000		All G values	$G \leq 60$ kg m^{-2} s^{-1}	$G > 60$ kg m^{-2} s^{-1}
Nusselt [43]	e_R [%]	44.45	18.48	83.40
	e_{AB} [%]	44.45	18.48	83.40
	σ_N [%]	45.9	9.39	51.30
Cavallini et al. [58] with Del Col et al. [59] correlation for τ_{wall}	e_R [%]	50.06	77.85	8.38
	e_{AB} [%]	51.31	78.25	10.92
	σ_N [%]	74.65	85.64	10.52
Cioncolini et al. [60] with Wallis [61] correlation for τ_{wall}	e_R [%]	4.96	17.35	−13.63
	e_{AB} [%]	28.10	37.43	14.11
	σ_N [%]	40.88	48.56	9.84

employed during the tests (chromatic confocal imaging and shadowgraph in one case, chromatic confocal imaging and interferometry in the other). Therefore, the measured liquid film thickness at the same vapor quality and mass flux basically does not depend on the condensation heat transfer process, but only on hydrodynamics, at least for the working conditions (for example, heat flux) of the present experiments.

- In the mass flux range from 70 to 150 kg m^{-2} s^{-1} the liquid film thickness of HFE-7000 is found to decrease with increasing mass flux and vapor quality. An increase of the liquid film thickness is observed when the mass flux increases from 30 kg m^{-2} s^{-1} to 50 kg m^{-2} s^{-1}, which can be due to the transition from shear stress driven to gravity driven downward flow condensation.
- High-amplitude waves with small frequency (15–18 Hz) are detected at both $G = 80$ kg m^{-2} s^{-1} and $G = 100$ kg m^{-2} s^{-1} with HFE-7000. Some vapor bubbles are found to be entrained in the liquid film by these high-amplitude waves, as evinced from flow visualizations.
- The experimental liquid film thickness results of HFE-7000 are compared by means of statistical and spectral analyses with those of R245fa and R134a, tested during previous experimental campaigns. HFE-7000 generally displays lower film thickness values compared to R245fa and R134a due to the smaller vapor density. At low mass flux (50 kg m^{-2} s^{-1}), the small liquid viscosity of R134a is responsible for the thinning of the liquid film with respect to the other fluids.
- The accuracy of available models for the prediction of the mean film thickness is assessed with comparison to the experimental data of HFE-7000. The model by Nusselt [43] provides the most accurate predictions of the mean liquid film thickness at the smallest mass flux, with mean absolute deviation between experimental and calculated values lower than 8.2% and 19.7% at $G = 20$ kg m^{-2} s^{-1} and $G = 30$ kg m^{-2} s^{-1}, respectively. This result confirms the very limited effect of the shear stress at the liquid–vapor interface at such low mass fluxes. Instead, the models of Cavallini et al. [58] and Cioncolini et al. [60] provide the best predictions of the mean film thickness at mass flux higher than 60 kg m^{-2} s^{-1} (mean absolute error equal to 10.9% and 14.1%, respectively).

Declaration of Competing Interest

The authors declare the following financial interests/personal relationships which may be considered as potential competing interests: [Davide Del Col reports financial support was provided by European

Space Agency (ESA). Marc Miscevic reports financial support was provided by European Space Agency (ESA).].

Data availability

Data will be made available on request.

Acknowledgements

The authors acknowledge the financial support of the European Space Agency (ESA) through the MAP Condensation program. The companies AERMEC SpA and Epsyl are acknowledged for funding a researcher and a PhD position, respectively.

References

[1] ISO, UNI EN ISO 4287-2009: Geometrical Product Specifications (GPS) – Surface texture: profile method – Terms, definitions and surface texture parameters., (2009).

[2] A. Cioncolini, J.R. Thome, Entrained liquid fraction prediction in adiabatic and evaporating annular two-phase flow, Nucl. Eng. Des. 243 (2012) 200–213, https://doi.org/10.1016/j.nucengdes.2011.11.014.

[3] I. Zadrazil, C.N. Markides, An experimental characterization of liquid films in downwards co-current gas-liquid annular flow by particle image and tracking velocimetry, Int. J. Multiph. Flow. 67 (2014) 42–53, https://doi.org/10.1016/j.ijmultiphaseflow.2014.08.007.

[4] B.J. Azzopardi, Disturbance wave frequencies, velocities and spacing in vertical annular two-phase flow, Nucl. Eng. Des. 92 (1986) 121–133.

[5] Y. Zhao, C.N. Markides, O.K. Matar, G.F. Hewitt, Disturbance wave development in two-phase gas-liquid upwards vertical annular flow, Int. J. Multiph. Flow. 55 (2013) 111–129, https://doi.org/10.1016/j.ijmultiphaseflow.2013.04.001.

[6] R.J. Belt, J.M.C. Van't Westende, H.M. Prasser, L.M. Portela, Time and spatially resolved measurements of interfacial waves in vertical annular flow, Int. J. Multiph. Flow. 36 (2010) 570–587. 10.1016/j.ijmultiphaseflow.2010.03.004.

[7] J. Vasques, A. Cherdantsev, M. Cherdantsev, S. Isaenkov, D. Hann, Comparison of disturbance wave parameters with flow orientation in vertical annular gas-liquid flows in a small pipe, Exp. Therm. Fluid Sci. 97 (2018) 484–501, https://doi.org/10.1016/j.expthermflusci.2018.03.020.

[8] S.V. Alekseenko, A.V. Cherdantsev, M.V. Cherdantsev, S.V. Isaenkov, D. M. Markovich, Study of formation and development of disturbance waves in annular gas-liquid flow, Int. J. Multiph. Flow. 77 (2015) 65–75, https://doi.org/10.1016/j.ijmultiphaseflow.2015.08.007.

[9] C.J. Martin, B.J. Azzopardi, Waves in vertical annular flow, Phys. Chem. Hydrodyn. 6 (1985) 257–265.

[10] A. Setyawan, Indarto, Deendarlianto, The effect of the fluid properties on the wave velocity and wave frequency of gas-liquid annular two-phase flow in a horizontal pipe, Exp. Therm. Fluid Sci. 71 (2016) 25–41, https://doi.org/10.1016/j.expthermflusci.2015.10.008.

[11] S. Jayanti, G.F. Hewitt, Hydrodynamics and heat transfer in wavy annular gas-liquid flow: A computational fluid dynamics study, Int. J. Heat Mass Transf. 40 (1997) 2445–2460, https://doi.org/10.1016/S0017-9310(96)00288-8.

[12] Y. Rivera, C. Berna, J.L. Muñoz-Cobo, A. Escrivá, Y. Córdova, Experiments in free falling and downward cocurrent annular flows – Characterization of liquid films and interfacial waves, Nucl. Eng. Des. 392 (2022), https://doi.org/10.1016/j.nucengdes.2022.111769.

[13] J.R. Thome, J. Kim, Encyclopedia of two-phase heat transfer and flow II. Special topics and applications, World Scientific, Singapore, 2016.

[14] T.A. Moreira, R.W. Morse, K.M. Dressler, G. Ribatski, A. Berson, Liquid-film thickness and disturbance-wave characterization in a vertical, upward, two-phase annular flow of saturated R245fa inside a rectangular channel, Int. J. Multiph. Flow. (2020), https://doi.org/10.1016/j.ijmultiphaseflow.2020.103412.

[15] P. Sawant, M. Ishii, T. Hazuku, T. Takamasa, M. Mori, Properties of disturbance waves in vertical annular two-phase flow, Nucl. Eng. Des. 238 (2008) 3528–3541, https://doi.org/10.1016/j.nucengdes.2008.06.013.

[16] G. Wang, Z. Dang, M. Ishii, Wave structure and velocity in vertical upward annular two-phase flow, Exp. Therm. Fluid Sci. 120 (2021), 110205, https://doi.org/10.1016/j.expthermflusci.2020.110205.

[17] F. Liang, Z. Fang, J. Chen, S. Sun, Investigating the Liquid Film Characteristics of Gas-Liquid Swirling Flow Using Ultrasound Doppler Velocimetry, AIChE J. 63 (2012) 2348–2357, https://doi.org/10.1002/aic.

[18] D. Schubring, A.C. Ashwood, T.A. Shedd, E.T. Hurlburt, Planar laser-induced fluorescence (PLIF) measurements of liquid film thickness in annular flow. Part I: Methods and data, Int. J. Multiph. Flow. 36 (2010) 815–824, https://doi.org/10.1016/j.ijmultiphaseflow.2010.05.007.

[19] A.V. Cherdantsev, J.S. An, A. Charogiannis, C.N. Markides, Simultaneous application of two laser-induced fluorescence approaches for film thickness measurements in annular gas-liquid flows, Int. J. Multiph. Flow. 119 (2019) 237–258, https://doi.org/10.1016/j.ijmultiphaseflow.2019.07.013.

[20] V. Voulgaropoulos, A. Patapas, S. Lecompte, A. Charogiannis, O.K. Matar, M. De Paepe, C.N. Markides, Simultaneous laser-induced fluorescence and capacitance probe measurement of downwards annular gas-liquid flows, Int. J. Multiph. Flow. 142 (2021), 103665, https://doi.org/10.1016/j.ijmultiphaseflow.2021.103665.

[21] D. Schubring, T.A. Shedd, E.T. Hurlburt, Studying disturbance waves in vertical annular flow with high-speed video, Int. J. Multiph. Flow. 36 (2010) 385–396, https://doi.org/10.1016/j.ijmultiphaseflow.2010.01.003.

[22] Y. Xue, C. Stewart, D. Kelly, D. Campbell, M. Gormley, Two-Phase Annular Flow in Vertical Pipes: A Critical Review of Current Research Techniques and Progress, Water (Switzerland). 14 (2022) 1–30, https://doi.org/10.3390/w14213496.

[23] C.B. Tibiriçá, F.J. do Nascimento, G. Ribatski, Film thickness measurement techniques applied to micro-scale two-phase flow systems, Exp. Therm. Fluid Sci. 34 (2010) 463–473. 10.1016/j.expthermflusci.2009.03.009.

[24] T.A. Moreira, V.E.C. Baptistella, G. Ribatski, Liquid-film thickness, flow pattern, and void fraction of hydrocarbons and their zeotropic mixtures during convective condensation, Int. J. Multiph. Flow. 159 (2023), 104341, https://doi.org/10.1016/j.ijmultiphaseflow.2022.104341.

[25] Y. Han, N. Shikazono, N. Kasagi, Measurement of liquid film thickness in a micro parallel channel with interferometer and laser focus displacement meter, Int. J. Multiph. Flow. 37 (2011) 36–45, https://doi.org/10.1016/j.ijmultiphaseflow.2010.08.010.

[26] Y. Han, H. Kanno, Y.J. Ahn, N. Shikazono, Measurement of liquid film thickness in micro tube annular flow, Int. J. Multiph. Flow. 73 (2015) 264–274, https://doi.org/10.1016/j.ijmultiphaseflow.2015.03.016.

[27] A. Donniacuo, R. Charnay, R. Mastrullo, A.W. Mauro, R. Revellin, Film thickness measurements for annular flow in minichannels: Description of the optical technique and experimental results, Exp. Therm. Fluid Sci. 69 (2015) 73–85, https://doi.org/10.1016/j.expthermflusci.2015.07.005.

[28] Y. Zhang, L. Jia, C. Dang, Z. Qi, Measurements of the liquid film thickness for annular flow during flow condensation in a circular tube, Int. J. Heat Mass Transf. 187 (2022), 122552, https://doi.org/10.1016/j.ijheatmasstransfer.2022.122552.

[29] A. Berto, P. Lavieille, M. Azzolin, S. Bortolin, M. Miscevic, D. Del Col, Liquid film thickness and heat transfer measurements during downflow condensation inside a small diameter tube, Int. J. Multiph. Flow. 140 (2021), 103649, https://doi.org/10.1016/j.ijmultiphaseflow.2021.103649.

[30] A. Berto, P. Lavieille, M. Azzolin, S. Bortolin, M. Miscevic, D. Del Col, Film thickness, interfacial waviness and heat transfer during downflow condensation of R134a, Appl. Therm. Eng. 214 (2022), 118808, https://doi.org/10.1016/j.applthermaleng.2022.118808.

[31] M. Beaumale, P. Lavieille, F. Topin, M. Miscevic, Simultaneous high-accuracy measurements of local heat transfer and phase distribution during convective condensation using non intrusive diagnostic tools, Exp. Therm. Fluid Sci. 141 (2023), 110801, https://doi.org/10.1016/j.expthermflusci.2022.110801.

[32] P. Toninelli, S. Bortolin, M. Azzolin, D. Del Col, Visualization and Numerical Simulations of Condensing Flow in Small Diameter Channels, Heat Transf. Eng. 40 (2019) 802–817, https://doi.org/10.1080/01457632.2018.1443255.

[33] A. Fershtman, L. Robers, H.M. Prasser, D. Barnea, L. Shemer, Interfacial structure of upward gas–liquid annular flow in inclined pipes, Int. J. Multiph. Flow. 132 (2020), 103437, https://doi.org/10.1016/j.ijmultiphaseflow.2020.103437.

[34] M. Azzolin, S. Bortolin, D. Del Col, Convective condensation at low mass flux: Effect of turbulence and tube orientation on the heat transfer, Int. J. Heat Mass Transf. 144 (2019) 1–38, https://doi.org/10.1016/j.ijheatmasstransfer.2019.118646.

[35] A. Berto, M. Azzolin, P. Lavieille, A. Glushchuk, P. Queeckers, S. Bortolin, C. S. Iorio, M. Miscevic, D. Del Col, Experimental investigation of liquid film thickness and heat transfer during condensation in microgravity, Int. J. Heat Mass Transf. 199 (2022), https://doi.org/10.1016/j.ijheatmasstransfer.2022.123467.

[36] E.W. Lemmon, I.H. Bell, M.L. Huber, M.O. McLinden, NIST Standard Reference Database 23: Reference Fluid Thermodynamic and Transport Properties (REFPROP), Version 10.0, National Institute of Standards and Technology, Standard Reference Data Program, Gaithersburg., 2018.

[37] Joint Committee for Guides in Metrology (JCGM), Evaluation of measurement data - Guide to the expression of uncertainty in measurement, Bur. Int. Des Poids Mes. (BIPM), Sèvres, Fr. (2008). http://www.bipm.org/en/publications/guides/gum.html (accessed October 29, 2019).

[38] L. Le Nguyen, Effect of gravity on convective condensation at low mass velocity, University Paul Sabatier, France) and University of Padova (Padova, Italy, Toulouse, 2017.

[39] M. Beaumale, Condensation convective: de l'analyse locale à l'établissement de lois de dimensionnement, University Paul Sabatier, Toulouse, France, 2022.

[40] R.K. Shah, A.L. London, Laminar Flow Forced Convection in Ducts: A Source Book for Compact Heat Exchanger Analytical Data, Academic Press, New York, 1978.

[41] P. Lavieille, M. Azzolin, A. Berto, P. Queeckers, A. Gluschuk, B. Schlegel, S. Bortolin, M. Miscevic, C.S. Iorio, D. Del Col, New measurement technique of liquid film thickness distribution with high spatial and temporal resolution: application to convective condensation in microgravity. In: Proceedings of 14th International Conference on Two-Phase Systems for Space and Ground Applications, Granada (Spain), 2019.

[42] B. Médéric, P. Lavieille, M. Miscevic, Void fraction invariance properties of condensation flow inside a capillary glass tube, Int. J. Multiph. Flow. 31 (2005) 1049–1058, https://doi.org/10.1016/j.ijmultiphaseflow.2005.06.004.

[43] W. Nusselt, Die oberflächenkondensation des wasserdampfes, Zeitschrift Des Vereines Dtsch. Ingenieure. 60 (1916) 541–546.

[44] D.B. Hann, A.V. Cherdantsev, B.J. Azzopardi, Study of bubbles entrapped into a gas-sheared liquid film, Int. J. Multiph. Flow. 108 (2018) 181–201, https://doi.org/10.1016/j.ijmultiphaseflow.2018.07.001.

[45] D.J. Rodríguez, T.A. Shedd, Entrainment of gas in the liquid film of horizontal, annular, two-phase flow, Int. J. Multiph. Flow. 30 (2004) 565–583, https://doi.org/10.1016/j.ijmultiphaseflow.2004.04.011.
[46] D.E. Woodmansee, T.J. Hanratty, Mechanism for the removal of droplets from a liquid surface by a parallel air flow, Chem. Eng. Sci. 24 (1969) 299–307, https://doi.org/10.1016/0009-2509(69)80038-2.
[47] A. Dasgupta, D.K. Chandraker, S. Kshirasagar, B.R. Reddy, R. Rajalakshmi, A. K. Nayak, S.P. Walker, P.K. Vijayan, G.F. Hewitt, Experimental investigation on dominant waves in upward air-water two-phase flow in churn and annular regime, Exp. Therm. Fluid Sci. 81 (2017) 147–163, https://doi.org/10.1016/j.expthermflusci.2016.10.012.
[48] R. Mesler, A mechanism supported by extensive experimental evidence to explain high heat fluxes observed during nucleate boiling, AIChE J. 22 (1976) 246–252, https://doi.org/10.1002/aic.690220204.
[49] P. Ju, X. Yang, Q. Zhu, Y. Yan, Y. Liu, M. Ishii, T. Hibiki, Prediction of flow distribution of vertical upward co-current adiabatic annular flow in 8 × 8 rod bundle, Ann. Nucl. Energy. 132 (2019) 555–562, https://doi.org/10.1016/j.anucene.2019.06.040.
[50] A.C. Ashwood, S.J. Vanden Hogen, M.A. Rodarte, C.R. Kopplin, D.J. Rodríguez, E. T. Hurlburt, T.A. Shedd, A multiphase, micro-scale PIV measurement technique for liquid film velocity measurements in annular two-phase flow, Int. J. Multiph. Flow. 68 (2015) 27–39, https://doi.org/10.1016/j.ijmultiphaseflow.2014.09.003.
[51] J.R. Thome, A. Cioncolini, Unified Modeling Suite for Two-Phase Flow, Convective Boiling, and Condensation in Macro-and Microchannels, Heat Transf. Eng. 37 (2016) 1148–1157, https://doi.org/10.1080/01457632.2015.1112212.
[52] Y. Rivera, J.L. Muñoz-Cobo, J.L. Cuadros, C. Berna, A. Escrivá, Experimental study of the effects produced by the changes of the liquid and gas superficial velocities and the surface tension on the interfacial waves and the film thickness in annular concurrent upward vertical flows, Exp. Therm. Fluid Sci. 120 (2021), https://doi.org/10.1016/j.expthermflusci.2020.110224.
[53] P. Ju, C.S. Brooks, M. Ishii, Y. Liu, T. Hibiki, Film thickness of vertical upward co-current adiabatic flow in pipes, Int. J. Heat Mass Transf. 89 (2015) 985–995, https://doi.org/10.1016/j.ijheatmasstransfer.2015.06.002.
[54] W.H. Henstock, T.J. Hanratty, The interfacial drag and the height of the wall layer in annular flows, AIChE J. 22 (1976) 990–1000, https://doi.org/10.1002/aic.690220607.
[55] M. Ishii, M.A. Grolmes, Inception criteria for droplet entrainment in two-phase concurrent film flow, AIChE J. 21 (1975) 308–318, https://doi.org/10.1002/aic.690210212.
[56] P.G. Kosky, F.W. Staub, Local Condensing Heat Transfer Coefficients in the Annular Flow Regime, AIChE J. 17 (1971) 1037–1043.
[57] D.F. Tatterson, J.C. Dallman, T.J. Hanratty, Drop sizes in annular gas-liquid flows, AIChE J. 23 (1977) 68–76, https://doi.org/10.1002/aic.690230112.
[58] A. Cavallini, G. Censi, D. Del Col, L. Doretti, G.A. Longo, L. Rossetto, A tube-in-tube water/zeotropic mixture condenser: Design procedure against experimental data, Exp. Therm. Fluid Sci. 25 (2002) 495–501, https://doi.org/10.1016/S0894-1777(01)00107-8.
[59] D. Del Col, A. Bisetto, M. Bortolato, D. Torresin, L. Rossetto, Experiments and updated model for two phase frictional pressure drop inside minichannels, Int. J. Heat Mass Transf. 67 (2013) 326–337, https://doi.org/10.1016/j.ijheatmasstransfer.2013.07.093.
[60] A. Cioncolini, D. Del Col, J.R. Thome, An indirect criterion for the laminar to turbulent flow transition in shear-driven annular liquid films, Int. J. Multiph. Flow. 75 (2015) 26–38, https://doi.org/10.1016/j.ijmultiphaseflow.2015.05.002.
[61] G.B. Wallis, One-dimensional two-phase flow, McGraw Hill, New York (USA), 1969.